

# Discovery of Small Ultra-short-period Planets Orbiting KG Dwarfs in Kepler Survey Using GPU Phase Folding and Deep Learning Detection System

Kaitlyn Wang<sup>1,2\*</sup>, Jian Ge<sup>3†</sup>, Kevin Willis<sup>1</sup>, Kevin Wang<sup>4</sup>, Yinan Zhao<sup>5</sup>

<sup>1</sup>Science Talent Training Center, Gainesville, FL, 32606 USA

<sup>2</sup>The Harker School, 500 Saratoga Ave, San Jose, CA 95129, USA

<sup>3</sup>Shanghai Astronomical Observatory, Shanghai 200030, China

<sup>4</sup>Princeton University, PO Box 430 Princeton, NJ 08544, USA

<sup>5</sup>Department of Astronomy, University of Geneva, Switzerland

Accepted XXX. Received YYY; in original form ZZZ

## ABSTRACT

Since the discovery of the first hot Jupiter orbiting a solar-type star, 51 Peg, in 1995, more than 4000 exoplanets have been identified using various observational techniques. Despite this, only a few hundred of these detected planets possess sub-Earth radii. The formation process of these sub-Earths remains elusive, and acquiring additional samples is essential for investigating this unique population. In our study, we employ a novel GPU Phase Folding algorithm combined with a Convolutional Neural Network algorithm, termed the GPFC method, on Kepler photometry data. This method enhances the transit search speed significantly over the traditional Box-fitting Least Squares method, allowing a complete search of the known Kepler KOI photometry data within hours using a commercial GPU card. To date, we have identified five promising sub-Earth short-period candidates: K00446.c, K01821.b, K01522.c, K03404.b, and K04978.b. A closer analysis reveals the following characteristics: K00446.c orbits a K dwarf on a 0.645091-day period. With a radius of 0.461  $R_{\oplus}$ , it ranks as the second smallest USP discovered to date. K01821.b is a sub-Earth with a radius of 0.648 $R_{\oplus}$ , orbiting a G dwarf over a 0.91978-day period. It is the second smallest USP among all confirmed USPs orbiting G dwarfs in the NASA Exoplanet Archive. K01522.c has a radius of 0.704  $R_{\oplus}$  and completes an orbit around a Sun-like G dwarf in 0.64672 days; K03404.b, with a radius of 0.738 $R_{\oplus}$ , orbits a Sun-like G dwarf on a 0.68074-day period; and K04978.b, with its planetary radius of 0.912 $R_{\oplus}$ , orbits a G dwarf, completing an orbit every 0.94197 days. Three of our finds, K01821.b, K01522.c and K03404.b, rank as the smallest planets among all confirmed USPs orbiting G dwarfs in the Kepler dataset. The discovery of these small exoplanets underscores the promising capability of the GPFC method for searching for small, new transiting exoplanets in photometry data from Kepler, TESS, and future space transit missions.

**Key words:** Algorithms – astronomy data analysis – deep learning – exoplanet detection – ultra-short-period planets – small planets – transit photometry – planetary systems formation

## 1 INTRODUCTION

Contrary to prevailing solar system-based planet formation theories, which do not predict planets with orbits significantly narrower than Mercury’s, ultra-short-period (USP) planets represent a captivating group of exoplanets with orbital periods of less than a day. These USPs may offer vital insights into the early evolution of planetary systems and the dynamics of star-planet interactions, including tidal forces and atmospheric erosion. The most extreme USPs, e.g. KOI1843.03 (K2-137b), have orbital periods of just 4 hours, teetering on the edge of tidal disruption (Rappaport et al. 2013; Smith et al. 2017). Found in approximately 0.5% of Sun-like stars, USPs typically have radii smaller than 2 $R_{\oplus}$  or, in the case of ultra-hot Jupiters,

greater than 10 $R_{\oplus}$  (Sanchis-Ojeda et al. 2014). Understanding how these planets achieve such short orbital periods remains one of the longest-standing unresolved problems in the field.

To date, three leading theories are proposed to explain the formation of ultra-short-period planets: in situ formation, migration driven by stellar tides, and tidal migration coupled with multi-body interactions (Adams et al. 2020). The in situ formation theory, which posits that these planets formed near their present orbits, is deemed less plausible due to the extreme temperatures these close-in orbits would encounter (Boss 1998). Moreover, given that host stars’ radii were significantly larger during their pre-main sequence phase compared to now (Palla & Stahl 1991; D’Antona & Mazzitelli 1994), USP planets in closer proximity would likely have been engulfed by the stars. Meanwhile, the role of tidal migration in the genesis of these planets remains an active area of investigation (Dawson & Johnson 2018). Given that USPs are often observed with outer accompanying

\* E-mail: 24kaitlynw@students.harker.org

† E-mail: jge@shao.ac.cn

planets in longer orbits, it is hypothesized that USP origins involve interactions among the sibling planets, which reposition USPs into their current positions closer to their host stars, possibly in orbits previously occupied by the stars themselves.

Regardless of its origin, once a planet settles into a short-period orbit, the host star’s influence may remove it in a few billion years. For volatile-rich planets, high atmospheric temperatures and intense stellar irradiation they endure can lead to atmospheric loss (Owen & Kollmeier 2019). Additionally, strong tidal forces can cause orbital decay, pushing these planets into a state of unstable Roche lobe overflow. Such destabilization can culminate in the complete disruption of their atmospheres after just a few orbits (Jia & Spruit 2016).

The main limitation in studying the enigmatic USP planets has been the scarcity of USP planets discovered so far. To date, there are only 43 USPs confirmed by the Kepler survey and 127 in the NASA confirmed planets archive. Assessing the relative abundance of USPs, including variations in orbital periods, planetary mass, the spectral type of their host stars, and the configurations of any associated multiplanet systems, is vital for testing theoretical models. However, the small sample size of known USPs means that current estimates of their occurrence rates are subject to large error margins. Therefore, expanding the USP data set is imperative for gaining a deeper understanding of this group.

In this paper, we present the discovery and detailed analysis of five short-period sub-Earth candidates—K00446.c, K01821.b, K01522.c, K03404.b, and K04978.b. Notably, K00446.c, which orbits a K dwarf with a period of 0.645091 days, is the second smallest USP planet detected so far, featuring a radius of  $0.461 R_{\oplus}$ . Among these discoveries, K01821.b, K01522.c, and K03404.b stand out as the smallest confirmed USPs orbiting G dwarfs in the Kepler dataset. Additionally, K01821.b, with its radius of  $0.648 R_{\oplus}$ , is the second smallest planet in the category of confirmed planets orbiting G dwarfs, as per the NASA Exoplanet Archive.

Our paper is organized as follows: Section 2 provides a brief overview of the GPU (Graphics Processing Units) Phase Folding and Convolutional Neural Network (GPFC) transit search method that led to these discoveries. Section 3 details our systematic approach to planet discovery, including the pre-processing of Kepler data, phase folding, and transit detection. In Section 4, we introduce our candidates, describing both the vetting and fitting processes used for validation and parameter determination. Section 5 delves into an in-depth discussion of the candidates’ characteristics. Finally, Section 6 explores future research directions and potential opportunities for follow-up observations.

## 2 OVERVIEW OF THE GPFC METHOD

The GPFC method, as detailed in Wang et al. (2023) and applied to the Kepler survey dataset, has facilitated the discovery of new USP planets presented in this paper. GPFC combines a novel Graphics Processing Unit (GPU) phase folding algorithm with a Convolutional Neural Network (CNN) to enhance transit detection. A key advantage of GPFC is its proficiency in detecting low Signal-to-Noise Ratio (SNR) planetary signals by processing raw light curves directly from the Kepler survey, independent of the TCE catalog. Meanwhile, GPFC operates at a speed three orders of magnitude faster than the predominant Box-fitting Least Squares (BLS) method, while also delivering higher precision. It outperforms BLS by achieving a higher true positive rate for the same false positive rate of detection and offers higher precision at the same recall rate. Furthermore, in a blind

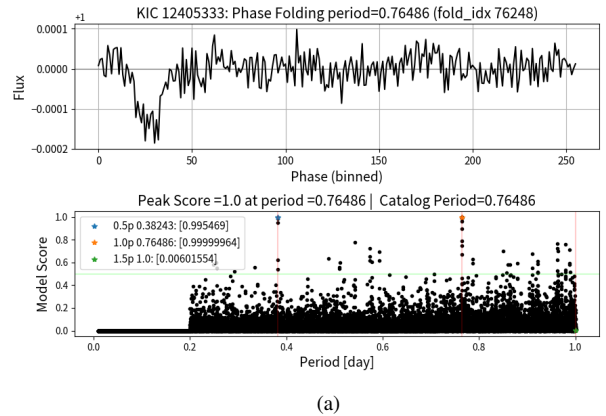


**Figure 1.** Kepler-1409b, as listed in the Kepler catalog, orbits its host star KID 12405333 with a period of 0.76486 days. This transit period has been precisely detected by the GPFC method. In the top panel, a clear light curve is visible in the folded light curve at this identified period of  $p=0.76486$  days. Meanwhile, the bottom panel reveals a peak CNN score of 0.99999964 at the same period, along with another notable score of 0.995469 at its harmonic half-period of  $p=0.38243$ .

search of *Kepler* light curves, GPFC successfully recovers 100% of known ultra-short-period planets.

The GPFC method comprises four main stages, specifically designed to identify transiting exoplanet candidates from time-domain surveys. Initially, raw light curves undergo preprocessing, which involves removing outliers and correcting for long-term stellar variability. Subsequently, these light curves are phase-folded at various trial periods that are evenly distributed across the USP search range of (0.2, 1] days, utilizing the GPU phase folding technique. The resultant folded curves are then normalized and fed into the CNN module. This module evaluates whether potential exoplanet transits exist at any of the trial periods. Light curves that receive high scores from the CNN module are further scrutinized in the vetting process.

We demonstrate the efficacy of the GPFC method using two Kepler objects from the Kepler Objects of Interest (KOI) catalog. First, KIC12405333: a star hosting a USP planet with an orbital period of 0.76486 days. As shown in Figure 1, the folded light curve generated by our method aligns with the transit period documented in the KOI catalog, yielding a peak CNN score of 0.99999964. The folded light curve prominently displays the transit-induced flux dip. In contrast, KIC12068975 is taken as an example which does not have any known planet transits within the range of (0.2, 1] days. By masking its recognized transit signal, we ensure no harmonics will interfere within our search range. Figure 2 presents the results: a peak CNN score of a mere 0.27934 and an absence of any discernible transit signal in the light curve at the folding period.

## 3 TRANSIT SEARCH PROCESS

In this section, we detail the approach employed by our GPFC system to discover Ultra-Short-Period (USP) exoplanets within the Kepler survey dataset.

### 3.1 Kepler Data Set Selection

Initially, light curves from the Q1–Q17 Kepler Data Release 25 (DR25) were retrieved, sourced from the Mikulski Archive for Space

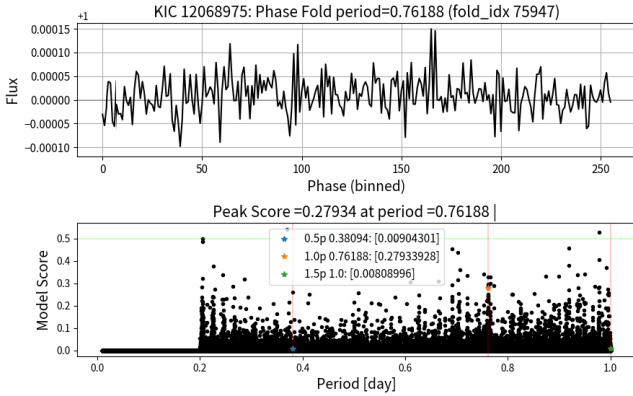


**Figure 2.** Depiction of the folded light curve for KIC12068975, which serves as an example where no transit is detected within our search range of (0.2, 1] days. The most prominent CNN score recorded is 0.27934 at a period of 0.76188 days, which is classified as a non-transit by the GPFC system.

Telescopes. Generated by the Kepler Science Processing Pipeline (Jenkins et al. 2010), these light curves contain integrated flux measurements taken at 1766-second intervals, spanning approximately four years and encompassing 30,000 to 70,000 epochs. Additionally, the Kepler Objects of Interest (KOIs) data set, as recorded in the NASA Exoplanet Archive as of June 2023, was also downloaded. This archive contained 9564 dispositioned KOIs, including 2350 confirmed planets, 2366 candidates, and 4848 false positives. For our analysis, we utilized transit parameters such as period, epoch, and duration from the KOI catalog to assist in light curve processing and transit verification.

We utilized the KOI catalog to filter our light curve dataset, deliberately excluding stars hosting planets designated as ‘False Positive’ or ‘Candidate’ in the Kepler disposition field. Our focus was solely on stars with all planets classified as ‘Confirmed’ or ‘Candidate’. This pre-selection strategy ensured that our dataset was free from the influence of secondary eclipses typically caused by eclipsing binaries. Such eclipses, not documented in the KOI catalog, could not be reliably masked and thus posed a risk of contaminating our analysis. By filtering out these stars, we substantially reduced the likelihood of false positive detection in our study.

### 3.2 Data Pre-processing

For each retrieved light curve, we performed pre-processing similar to the procedure outlined in (Vanderburg & Johnson 2014; Shallue & Vanderburg 2018). Initially, we flattened the light curve by iteratively fitting it with a b-spline, masking all confirmed transits. During this process,  $3\sigma$  outliers were progressively discarded. Subsequently, the light curve was divided by the best-fit spline. We then produced a “no-transit” light curve by excluding all known planet transits listed in the KOI catalog, priming the light curve for potential new planet discoveries. This no-transit curve served as the input for our fast GPU phase folding module.

### 3.3 Fast GPU Phase Folding

Our fast GPU phase folding module accepts a no-transit light curve and performs phase folding on it. Given the absence of prior knowledge regarding a potential transit’s period, we sampled 100,000 trial periods across our period search range. For USP planet detection, our

**Table 1.** Candidates List

KOI Name	Host KIC	Period (days)	CNN Score	SNR	FAP (%)
K01821.b	8832512	0.91978	0.93092	7.3	0.118
K03404.b	8409295	0.68074	0.55994	6.2	0.463
K00446.c	4633570	0.64509	0.89182	6.5	0.700
K01522.c	12266636	0.64672	0.96498	6.3	0.792
K04978.b	3428127	0.94197	0.83083	6.9	0.922

study concentrated on the USP period range of (0.2, 1] days, though the methodology can be adapted to different ranges. Using the GPU phase folding algorithm, the no-transit curve is folded and binned for each of the 100,000 periods, yielding 100,000 folded results, each being 256 in length post-binning. The high precision of folding is pivotal to the search’s success since minor signals from shallow transits can be easily obscured with a slight time deviation. The GPU’s grid system enables the simultaneous folding of the 100,000 trial periods, requiring approximately 5 seconds to fold a single curve with around 7000 data points.

### 3.4 Noise Normalization

Upon getting the 100,000 folded outcomes from the GPU Phase Folding module, we applied a noise normalization on them to uniform the standard deviation across all folded light curves, prepping them for the Convolutional Neural Network module.

### 3.5 Convolutional Neural Network

Subsequently, we fed the 100,000 folds into our CNN module, which has been specifically fine-tuned to identify USP transit signals typical of Kepler light curves. Our training data comprised two million synthetic light curves: one million with positive USP transit signals and another million without, based on genuine USP parameter distributions from the Kepler dataset. Post-training, the best-performing model achieved an accuracy rate of 94.6%. We utilized the Adam optimization algorithm (Kingma & Ba 2014) to minimize the cross-entropy error function, with a learning rate set at  $10^{-6}$  and a batch size of 32 across 90 epochs. Recognizing that the CNN might also pick up weaker peaks related to the harmonics of the transit period, we integrated the CNN scores with a harmonics check to confirm the existence of a transit event.

## 4 RESULTS

Upon completing the validation process for transit events flagged with high confidence by the CNN module, we identified five robust candidates, as listed in Table 1. The selection of these candidates hinged on two key criteria: firstly, they each achieved high scores from the CNN module, surpassing a defined threshold of 0.5. Secondly, the potential of these candidates as genuine transiting exoplanets was validated through a rigorous vetting process, the specifics of which are detailed in the subsequent section.

### 4.1 Candidate Vetting Process

In this study, we subjected potential exoplanet candidates to a comprehensive vetting process comprising eleven tests, as detailed below.

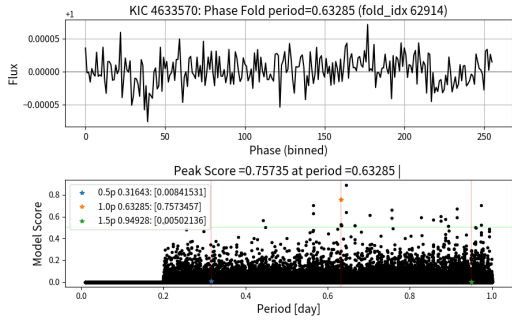


**Figure 3.** Folded light curve and CNN scores for candidate K00446.c, host star KIC4633570. Within USP period range (0.2,1] day, a transit is detected at period  $p=0.6451$  with a CNN score of 0.89182 and SNR 6.5.

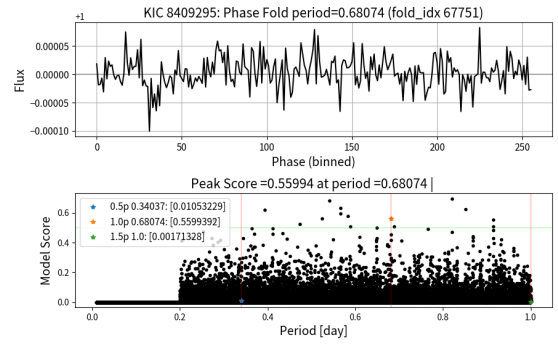


**Figure 6.** Folded light curve and CNN scores for candidate K03404.b, host star KIC8409295. Within USP period range (0.2,1] day, a transit is detected at period  $p=0.68074$  with a CNN score of 0.55994 and SNR 6.2.

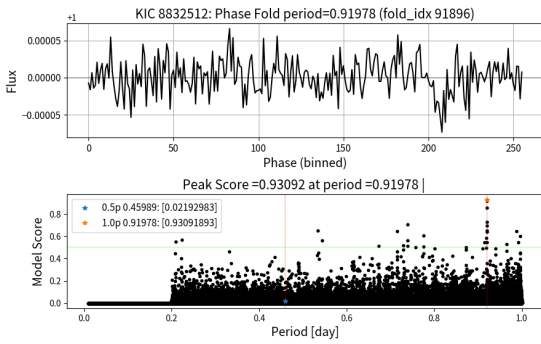


**Figure 4.** Folded light curve and CNN scores for candidate K01821.b, host star KIC8832512. Within USP period range (0.2,1] day, a transit is detected at period  $p=0.9198$  with a CNN score of 0.93092 and SNR 7.3.

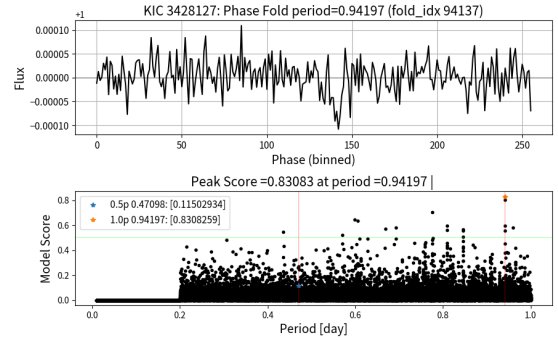


**Figure 7.** Folded light curve and CNN scores for candidate K04978.b, host star KIC3428127. Within USP period range (0.2,1] day, a transit is detected at period  $p=0.94197$  with a CNN score of 0.83083 and SNR 6.9.

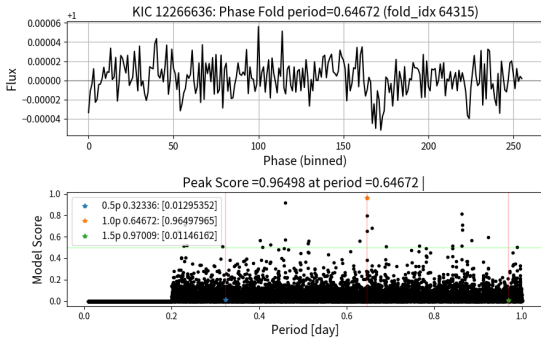


**Figure 5.** Folded light curve and CNN scores for candidate K01522.c, host star KIC12266636. Within USP period range (0.2,1] day, a transit is detected at period  $p=0.64672$  with a CNN score of 0.96498 and SNR 6.3.

The tests are compiled from [Kepler Data Validation Documentation](#) in the NASA Exoplanet Archive, relevant previous literature ([Shallue & Vanderburg 2018](#); [Shahaf et al. 2022](#); [Adams et al. 2021](#)), and our own methods. As an illustrative example, we demonstrate the vetting results for candidate K01821.b throughout this section while providing results for all other candidates in the Appendix.

### 1. Neighbor Star Contamination Harmonics Check

We first investigated the possibility of the transit signal arising from contamination by nearby stars ([Shallue & Vanderburg 2018](#)). By

extracting Target Pixel File (TPF) images from the Kepler Community Follow-up Program (CFOP), we verified that none of the host stars—KIC4633570, KIC8832512, KIC12266636, KIC8409295, or KIC3428127—had neighboring stars within 20 arcseconds that could be of concern. Figure 8 showcases the seasonal TPFs, FFI, and UKIRT-J plots for K01821.b.

### 2. Secondary Eclipse Check

We examined the phase-folded light curves for evidence of secondary eclipses, which could suggest that the transit signal originates from an eclipsing binary rather than a planet ([Shallue & Vanderburg 2018](#)). After masking known TCEs and phase-folding based on the orbital period, a search for the primary eclipse was undertaken using BLS. No eclipses were discernible for any of the host stars—KIC4633570, KIC8832512, KIC12266636, KIC8409295, or KIC3428127.

### 3. BLS Peaks Check

We next utilized the BLS periodogram on the light curves to examine BLS peaks. For all relevant host stars—KIC4633570, KIC8832512, KIC12266636, KIC8409295, and KIC3428127—a focused search range aligned with their identified transit periods revealed the transits manifesting as minor peaks in the BLS periodograms. However, these peaks were not prominent enough to be flagged by BLS.

### 4. Known Sibling Transit Harmonics Check

We subsequently explored whether the detected transit period could be a product of harmonic residuals—either integral multiples or fractions of the genuine period—of other sibling planets present within the host star’s system. All candidates under consideration exhibited



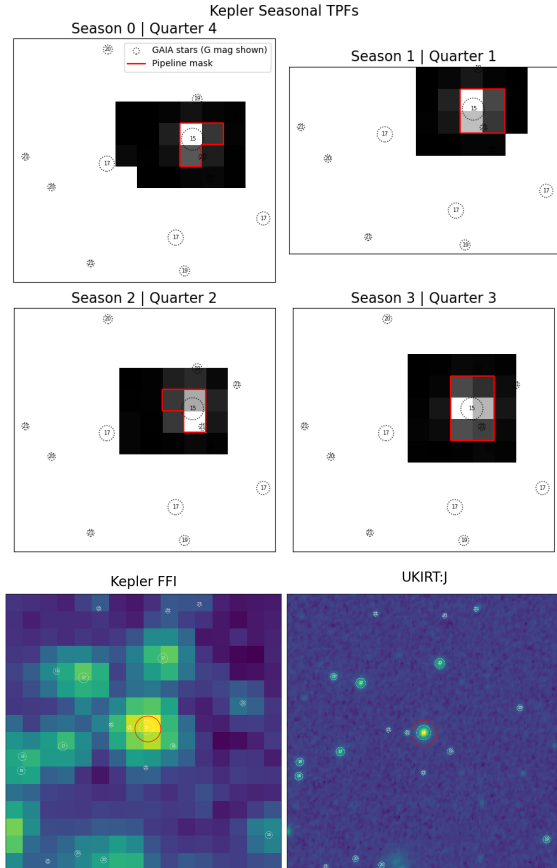


**Figure 8.** The seasonal Target Pixel Files (TPF), Full-field Images (FFI) and UKIRT-J plots for candidate K01821.b. The upper four seasonal TPFs show the position and apparent magnitude of the neighboring stars. Stars located within the highlighted red aperture exhibit significantly higher magnitudes, indicating lower brightness. This ensures that they do not contribute to any interference with the detected transit signal. The FFI and UKIRT-J images below allow a visual inspection of the broader view of the field with no contamination exhibited.

transit periods distinct from any potential harmonics. Figure 9 depicts the peaks discerned via the BLS methodology, juxtaposed with the known transit harmonics check for K01821.b.

### 5. Even-odd Transits Check

Following this, we carried out the even-odd transit examination by folding only on either even-numbered transits or odd-numbered transits (Shallue & Vanderburg 2018). Our verification revealed that the transit signals for each candidate were uniformly observed in both odd and even groupings. Furthermore, the transit depths,  $t_0$ , and their profiles remained consistent throughout. This diagnostic serves to rule out potential false positives stemming from instrumental anomalies. Figure 10 showcases this even-odd transit scrutiny for candidate K01821.b.

### 6. Left-half and Right-half Transits Check

Through the left-right transit examination, we ascertained a uniformity in the transit signals across the duration of Kepler’s mission for all of our candidates. This evaluation is instrumental in identifying and negating interference attributed to the “column anomaly”—a scenario where a star with varying luminosity, located on the identical CCD column as the primary target, may infuse unwanted signals during the readout process (Coughlin et al. 2016). Our study found no traces of such column anomalies in any candidate data. Figure

11 provides a visualization of this left-right transit assessment for K01821.b.

### 7. Quarterly Rotation Check

Throughout its primary mission, Kepler underwent periodic recalibrations, approximately every 90 days, to ensure its solar panels remained oriented towards the Sun. This necessitated that stars were re-positioned on different segments of the CCD array (Shallue & Vanderburg 2018). Sometimes, contamination signals could be introduced into the light curve more strongly in some positions on the CCD than others, causing differences in the strength and depth of transit signals on each CCD. We checked that the transit signals did not change significantly depending on which CCD module the target stars were observed. Figure 12 illustrates this quarter-consistency check for candidate K01821.b.

### 8. Bootstrap Validation

We performed a bootstrap validation similar to the one used in Shahaf et al. (2022). For each candidate raw light curve, we injected random time intervals between its consecutive quarters, with the intervals selected in the range from 0 to the detected transit period specific to the candidate. Post this temporal perturbation, we fed the time-shifted light curve into our GPU-based folding and CNN processing pipeline to find the most prominent periodogram peak and subsequently computed its SNR. This procedure was repeated a total of ten times for each target, allowing us to determine the mean SNR and its corresponding standard deviation across the ten iterations. In setting our validation criteria, we mandated that the SNR associated with the detected transit should be larger than four times the standard deviation gleaned from the ten bootstraps. All of our candidates passed this bootstrap validation criterion.

### 9. Inversion Validation

To further differentiate the transit signals from non-planetary sinusoidal or alike periodic signals, we performed an inversion test by inverting flux values around their nominal baseline thus converting the troughs of a light curve into crests and vice versa (Adams et al. 2021). Given that our pre-processing step ensures that the average flux value of a normalized light curve equals to 1, the inversion process generates a new light curve with its flux values equal to 2 minus their original values. The inverted light curve was then processed by our GPU folding and the CNN pipeline to discern the potential presence of a transit signal. To the end, none of the inverted light curves of our candidates displayed signals close to their detected transit periods therefore passing the inversion test.

### 10. Outside Apertures Check

In order to ensure that the transit signals were not the result of contaminations from scattered background light, we undertook an outside apertures test (Shallue & Vanderburg 2018). For each candidate under consideration, we constructed light curves derived from pixels situated outside the optimal Kepler aperture. These light curves were subsequently folded based on their respective detected transit periods. Should the transit signals emanating from the background be significantly more pronounced than those from the on-target pixels, it would be indicative of potential contamination. Our test results showed no significant signals, which proved the transit signals have their source on or near the target star.

### 11. False Alarm Probability Check

The False Alarm Probability is a valuable tool when vetting transiting exoplanet candidates found in light curve data. In essence, it provides the probability that a transit-like signal was produced by noise correlation. This metric has been around for decades (SOURCE) and there are many studies and implementations that can be found in literature.

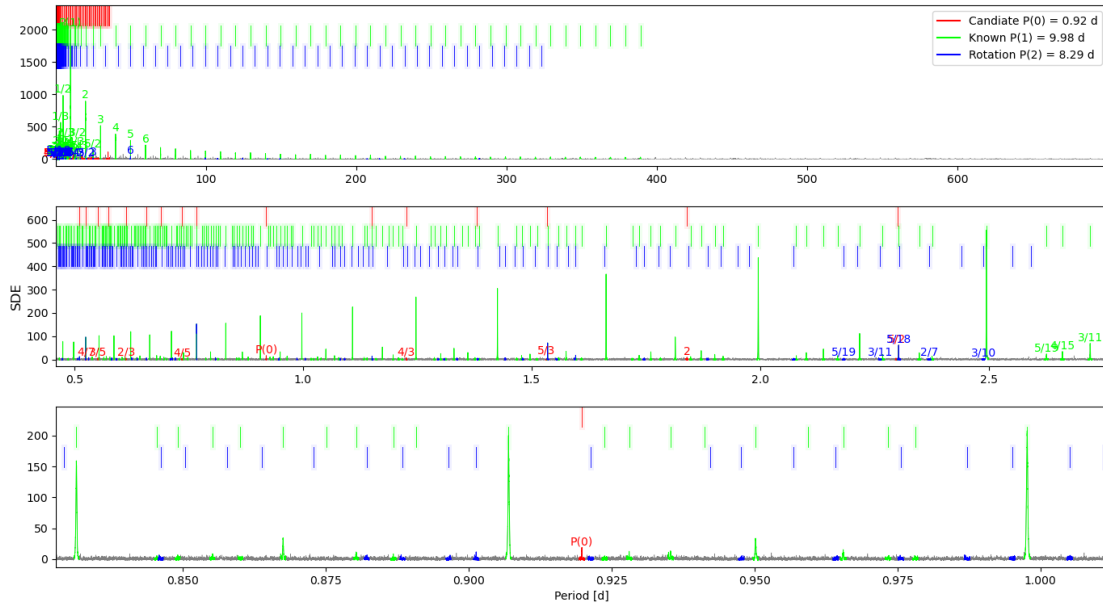


**Figure 9.** This figure presents the BLS Peaks Check and Known Sibling Transit Harmonics Check for candidate K01821.b. Harmonics of the orbital period for the host star’s known orbiting planet are color-coded in green. Harmonics associated with the rotational period of the variable star are indicated in blue. Meanwhile, the harmonics of the orbital period of the new candidate are marked in red. This visualization confirms that the orbital period of the new candidate does not coincide with the periods of the already known planet or the rotational period of the star.

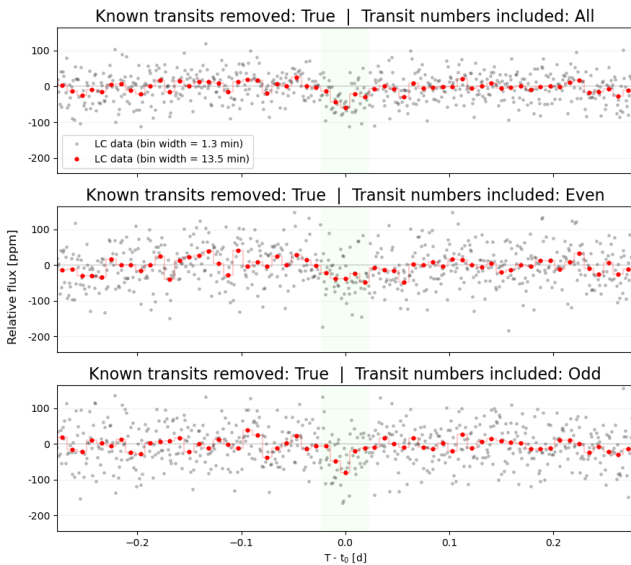


**Figure 10.** Even-odd Transit Check for candidate K01821.b. This test verifies that the transit signals of the new candidates remain consistent across both subsets of the light curve time sequence.

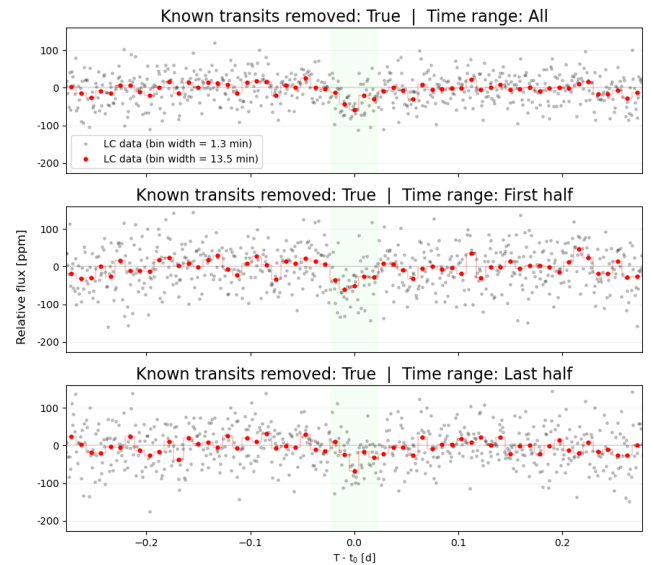


**Figure 11.** Left-half and Right-half Transit Check for candidate K01821.b. This test verifies that the transit signals of the new candidates remain consistent across both subsets of the light curve time sequence.

The Transit Least Squares (TLS) algorithm (Hippke & Heller 2019) is pivotal in our methodology, serving as the backbone for the evaluation of light curve data. Upon input of a light curve, TLS generates a spectrum of Signal Detection Efficiency (SDE) scores, each corresponding to a distinct orbital period. The utility of SDEs in FAP calculations is twofold: they are both noise-normalized and deterministic. This characteristic is crucial, given the diverse signal-to-noise ratios (SNRs) encountered in light curves. Noise normalization ensures that the SDE metric is consistent across varying SNR levels,

facilitating the development of a universal model for the FAP relationship. Additionally, the deterministic nature of SDEs, derived directly from empirical light curve data, allows for consistent SDE values for a specific transit signal across different light curves, assuming comparable SNR. This consistency is achievable through precise configuration of the TLS settings, reinforcing the reliability of SDE as a robust metric in our analysis.

The construction of the FAP statistic commenced with the selection of four KOIs, from which all known transit signals were removed,

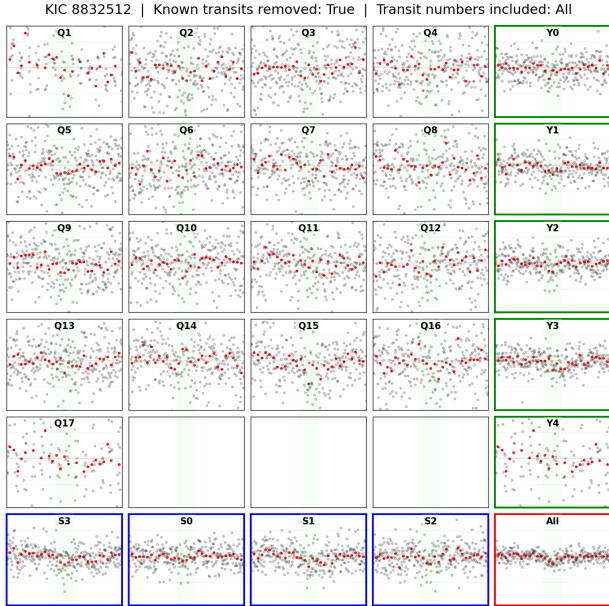


**Figure 12.** Quarterly Rotation Check for candidate K01821.b. This test confirms the consistency of the transit signals across different quarters.

followed by a detrending process of the light curves. Leveraging these detrended baselines, we generated 250 bootstrap replicas for each, culminating in a dataset of 1000 synthetic light curves. These were then analyzed using the TLS algorithm, which provided SDE scores across specified orbital periods. Our search, concentrated on USP planets, dictated the confinement of TLS processing to an orbital period range of (0.2, 1] day. The maximal SDE value extracted from each light curve formed a dataset of 1000 SDEs. From this, we constructed a Cumulative Distribution Function (CDF), delineating the relationship between SDE and 1-FAP. Further analysis involved fitting the Probability Distribution Function (PDF) of these SDEs with a log-normal distribution, which yielded an exemplary fit (PROVIDE MEASURE OF FIT). This log-normal model of the PDF was then transformed into a CDF model, establishing a smooth and continuous correlation between SDE and 1-FAP. Finally, we calculated the FAP values by subtracting the 1-FAP percentages from unity, thereby deriving the definitive SDE-FAP relationship model for our study.

With the SDE-FAP model solved, we could then obtain FAP values for our candidates by simply running the detrended light curves through TLS to obtain the SDE of the candidate transit signal, then use the SDE-FAP model to obtain the FAP estimate.

For verification of the SDE-FAP model we used synthetic light curves with pure white-noise to produce the SDE-FAP relationship. To do this we produced 1000 light curves consisting of pure white-noise. The SNR of each these light curves was set by drawing a random SNR from a uniform distribution of values representing the range of SNRs seen in real Kepler light curves. These light curves were then inputted to the GTLS algorithm which provided the SDE-period spectra. The GTLS software was configured to only evaluate the period range of (0.2, 1.0] day. The maximum SDE of each light curve was then used to produce a PDF to which a log-normal model was fit.

In the final verification step of the SDE-FAP relationship model, we used the light curves of our candidates to produce a new SDE-FAP model. This step was taken to ensure that the model still holds true for these targets which would indicate that the candidate transit signals

we found were likely not produced by red noise. This test procedure was identical to that which we used to construct the original SDE-FAP model. That is, for each light curve, we removed all known transits then detrended. Then each light curve was bootstrapped to produce 250 new light curves. After using GTLS and producing the log-normal fit to the PDF of the SDE maximums, we derived a SDE-FAP relationship model for each candidate.

Upon analyzing Kepler data, we observed that both confirmed and candidate USPs consistently have an FAP of less than 1%. Guided by this criterion, we retain our candidates only whose detected-transit FAP fell below this threshold. The FAP values associated with our candidates are systematically cataloged in Table 1.

Through the initial ten vetting tests mentioned above, we narrowed down the field from approximately 40 candidates to 12. Following the False Alarm Probability (FAP) check, this number was further refined, finalizing our list to 5 candidates.

## 4.2 Candidate Fitting Process

Next, we fitted the raw Kepler light curves of the candidates with Mandel & Agol (2002) model to determine the planet and orbital parameters of the candidates. The parameter space was explored using the Markov Chain Monte Carlo (MCMC) algorithm (Goodman & Weare 2010). Through iterative MCMC simulations, the orbital period, time of transit, orbital inclination, scaled semimajor axes, planet/host radius ratios, and quadratic limb darkening coefficients following the parameters of (Kipping 2013) of the candidates were confined. Gaussian priors were imposed on the two limb-darkening coefficients, centered at values predicted by (Claret, A. & Bloemen, S. 2011) for the host stars, and convergence of the MCMC chains was tested based on maximum likelihood estimation (MLE). The MCMC fitting results for candidate KIC8832512 are illustrated in Figure 13 and the corner plot is shown in Figure 14. The Appendix section contains the MCMC plots for all other candidates.

Table 2 shows the derived MCMC parameters of our candidates.

Through MCMC fitting, several planetary characteristics of our candidates are determined.

K00446.c has a radius approximately  $0.461 R_{\oplus}$  and is inclined at  $90.06^{\circ}$  from Earth's reference point. Hosted by KIC4633570, a K-type main sequence star with a mass of  $0.656 M_{\odot}$  and a size of  $0.668 R_{\odot}$ , this discovery turns KIC4633570 into a three-planet multiplanetary system. Currently, the system boasts two confirmed planets: Kepler-158b (radius:  $2.27 R_{\oplus}$ , orbital period: 16.709206 days) and Kepler-158c (radius:  $1.97 R_{\oplus}$ , orbital period: 28.55158 days). Kepler-158d, with its short 0.645091-day orbit, is the system's smallest and innermost planet.

K01821.b possesses a radius of  $0.648 R_{\oplus}$  and is inclined at  $89.86^{\circ}$  from Earth's reference point. Its host, KIC8832512, is a G-type main sequence star with attributes  $0.821 M_{\odot}$  in mass and  $0.928 R_{\odot}$  in size. The planet's addition makes KIC8832512 a two-planet system, accompanying a previously confirmed planet with a 9.97682-day orbit.

K01522.c, with a radius of  $0.704 R_{\oplus}$ , inclines at  $89.38^{\circ}$  from Earth's reference point. It orbits KIC12266636, a Sun-like G-type star (mass:  $0.974 M_{\odot}$ , size:  $1.022 R_{\odot}$ ). This finding turns KIC12266636 into a three-planet system, having two other planets with orbital periods of 12.654896 and 33.3856176 days, respectively.

K03404.b features a radius of  $0.738 R_{\oplus}$  and an inclination of  $90.02^{\circ}$  from Earth's reference point. It circles KIC8409295, a Sun-like G-type main sequence star (mass:  $0.977 M_{\odot}$ , size:  $0.957 R_{\odot}$ ). Its discovery supplements an already confirmed planet in the system

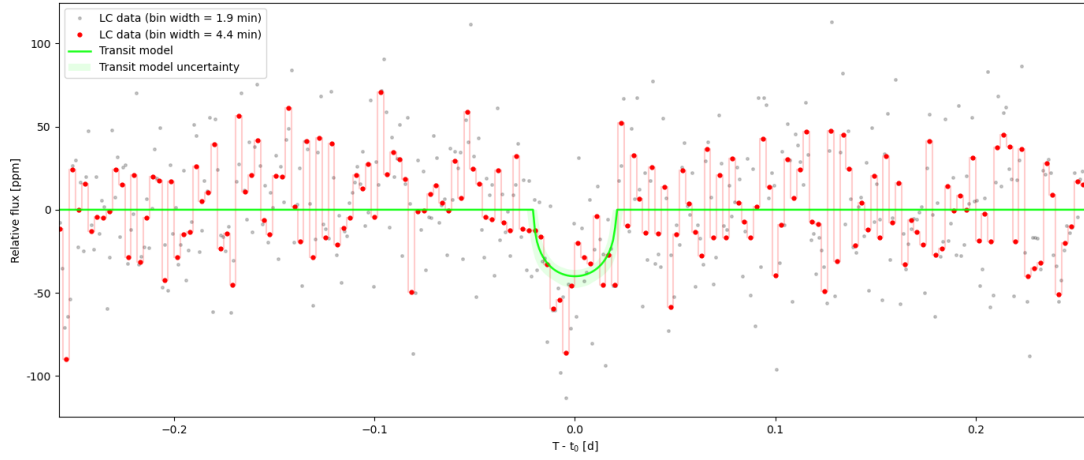


**Figure 13.** MCMC best-fitting plot for candidate K01821.b. The flux data are folded with the transit period and then binned into 1.9-minute bins (shown as grey dots), and 2-minute intervals (shown as red lines). The green curve represents the best-fitting transit model, with the green shaded area in the transit window indicating the uncertainty of the model.

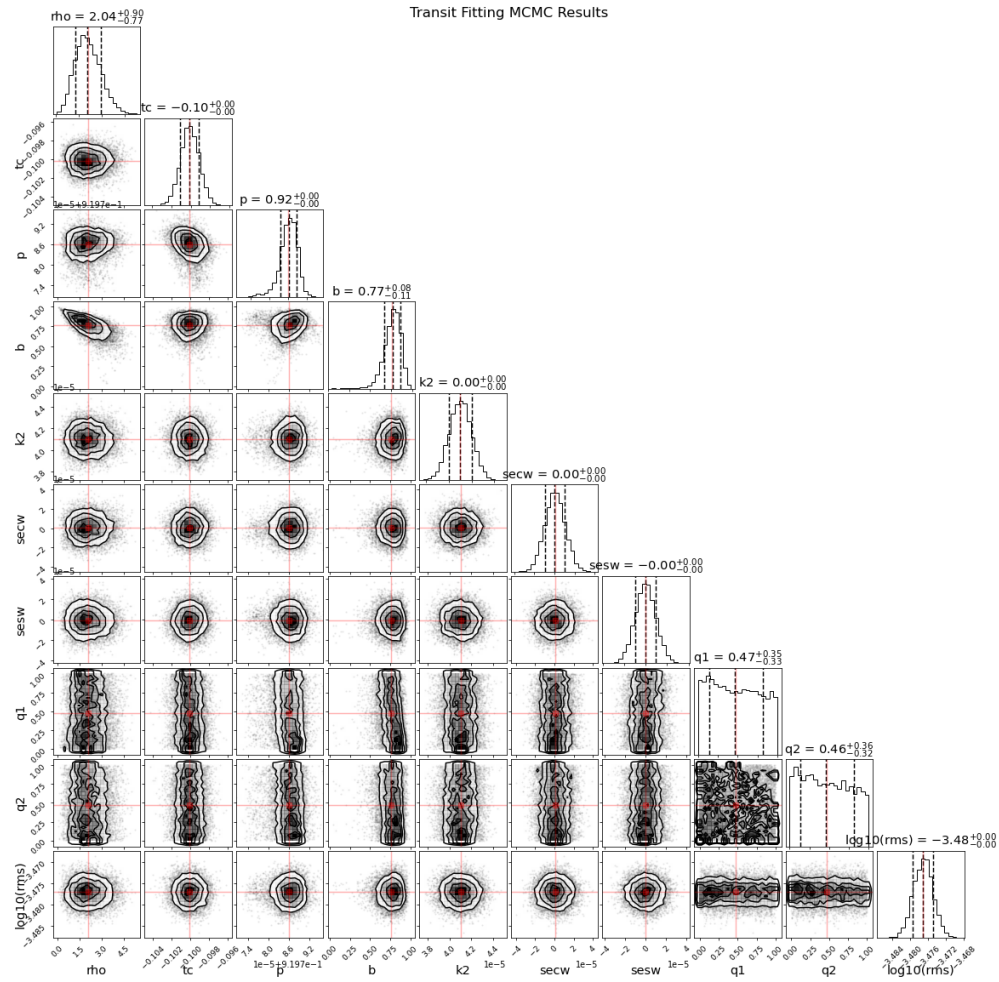


**Figure 14.** MCMC fitting corner plot for candidate K01821.b. Indicated are the stellar density ( $\rho$ ), time of central transit ( $t_c$ ), orbital period ( $p$ ), impact parameter ( $b$ ), square of the radius ratio ( $k_2$ ), orbit periastron and eccentricity params ( $secw$  and  $sesw$ ), limb-darkening coefficients ( $q_1$  and  $q_2$ ), as well as the logarithm base 10 of the white noise level in the data ( $\log_{10}(rms)$ ). The red lines represent the most likely values, while the dashed lines reflect the one sigma limits.



**Table 2.** Stellar and Planetary Parameters of our Candidates. Stellar and planetary orbital parameters including orbital period, time of transit, semi-major axis, orbital inclination, radius and radius ratio are listed in this table. K00446.c with radius  $0.461R_{\oplus}$  orbits KIC4633570 (spectral type K) over a period of 0.645091 days; K01821.b with radius  $0.648R_{\oplus}$  orbits KIC8832512 (spectral type G) over a period of 0.91978 days; K01522.c with radius  $0.704R_{\oplus}$  orbits KIC12266636 (spectral type G) over a period of 0.68074 days; K03404.b with radius  $0.738R_{\oplus}$  orbits KIC8409295 (spectral type G) over a period of 0.68074 days; K04978.b with radius  $0.912R_{\oplus}$  orbits KIC3428127 (spectral type G) over a period of 0.94197 days.

Stellar Parameters	KIC4633570	KIC8832512	KIC12266636	KIC8409295	KIC3428127
Teff[K] (Gaia)	4895.97 [K]	5169.47 [G]	5456.75 [G]	5565.53 [G]	5050.28 [G]
Mass [ $M_{\odot}$ ]	$0.656^{+0.073}_{-0.049}$	$0.821^{+0.12}_{-0.065}$	$0.974^{+0.127}_{-0.104}$	$0.977^{+0.05}_{-0.062}$	$0.859^{+0.126}_{-0.065}$
Radius [ $R_{\odot}$ ]	$0.668^{+0.054}_{-0.059}$	$0.928^{+0.239}_{-0.147}$	$1.022^{+0.288}_{-0.155}$	$0.957^{+0.132}_{-0.066}$	$0.966^{+0.385}_{-0.133}$
Derived Planet Parameters	K00446.c	K01821.b	K01522.c	K03404.b	K04978.b (-)
Transit Time[BKJD]	$0.05990^{+0.001}_{-0.001}$	$-0.10010^{+0.001}_{-0.001}$	$0.20^{+0.001}_{-0.001}$	$-0.05980^{+0.001}_{-0.001}$	$-0.0999^{+0.0009}_{-0.0009}$
Period[day]	$0.6450840^{+2e-06}_{-2e-06}$	$0.9197860^{+3e-06}_{-3e-06}$	$0.6467170^{+2e-06}_{-2e-06}$	$0.6807500^{+1e-06}_{-1e-06}$	$0.9419660^{+2e-06}_{-2e-06}$
Semi-major axis [ $R_{\odot}$ ]	$4.2^{+0.4}_{-0.4}$	$4.5^{+0.6}_{-0.6}$	$3.1^{+0.6}_{-0.6}$	$3.8^{+0.5}_{-0.5}$	$4.6^{+0.6}_{-0.6}$
Inclination[rad]	$1.39^{+0.04}_{-0.04}$	$1.39^{+0.05}_{-0.05}$	$1.27^{+0.09}_{-0.09}$	$1.33^{+0.05}_{-0.05}$	$1.37^{+0.04}_{-0.04}$
Radius [ $R_{\oplus}$ ]	$0.461^{+0.006}_{-0.006}$	$0.648^{+0.008}_{-0.008}$	$0.704^{+0.009}_{-0.009}$	$0.738^{+0.007}_{-0.007}$	$0.912^{+0.006}_{-0.006}$

with an 82.292865-day orbit, marking KIC8409295 as a two-planet system.

Lastly, K04978.b's radius measures at  $0.912R_{\oplus}$  with an inclination of  $90.07^{\circ}$ . Its host, KIC3428127, is a G-type main sequence star characterized by a mass of  $0.859M_{\odot}$  and a size of  $0.966R_{\odot}$ . This discovery complements another confirmed planet with an orbital period of 339.18998 days, categorizing KIC3428127 as a two-planet system.

## 5 DISCUSSIONS

In this section, we delve into a comprehensive analysis of our identified candidates, examining their distribution in the backdrop of all USP planets discovered by the Kepler survey. We further discuss the implications of our findings in relation to host star spectral types, the broader framework of multi-planetary systems, and prevailing star formation theories.

### 5.1 Period Radius Distribution

Figure 15 illustrates the period distribution for all confirmed USPs in the NASA Exoplanet Archive which reveals that our identified candidates predominantly belong to the category of exoplanets with small, sub-Earth radii. This highlights the high sensitivity of the GPFC method and its ability to detect small planets which may have eluded earlier searches.

K00446.c, with a radius of  $0.461R_{\oplus}$ , emerges as the second smallest USP planet when compared with both Kepler and NASA's roster of confirmed exoplanets. Its host, KIC4633570, is identifiable as a K-type star, marked by an effective stellar temperature of  $4895.97K$  as cataloged in the GAIA Archive (Gaia Collaboration et al. 2021).

K01821.b, with its radius of  $0.648R_{\oplus}$ , along with K01522.c possessing radii of  $0.704R_{\oplus}$  and  $0.738R_{\oplus}$  respectively, become the three smallest USPs orbiting G-type stars within the Kepler's confirmed USP discoveries. Furthermore, K01821.b ranks the second smallest USP with a G-type star host among NASA's confirmed exoplanets.

Figure 16 illustrates the period distribution for all confirmed Ke-

**Table 3.** USP occurrence rate vs stellar spectral type among NASA confirmed exoplanets.

Stellar Type	USP Occurrence rate
F	0.7%
G	2.2%
K	3.1%
M	8.0%

pler USPs, including the categorized distributions based on host stellar types.

### 5.2 Occurrence Rate vs. Stellar Type

We explored the relationship between the occurrence rate of USPs and the spectral type of their host stars. Based on Kepler data, (Sanchis-Ojeda et al. 2014) deduced that M-dwarfs are roughly 10 times more likely than F-dwarfs to host a USP planet with a radius double that of Earth's. Diving deeper into the NASA confirmed planet archive, we corroborated that the occurrence rate of USPs diminishes as the host star's effective temperature rises (as detailed in Table 3). A noteworthy statistic reveals that while 0.7% of confirmed USP planets in the NASA archive orbit F-type stars, a significant 8.0% revolve around M-type stars, marking them as ten times more prevalent. Our findings introduce an additional USP in the vicinity of a K-type star and four in the orbit of G-type stars, presenting valuable data for follow up investigation.

### 5.3 Multiplanet Systems

Each planet we identified resides in a system already known to harbor at least one other planet. Specifically, the planets we discovered are consistently the innermost members of their respective systems and possess the smallest radii.

The NASA Confirmed Exoplanet Archives present that 29.5% of USPs have at least one sibling planet, and 11.5% have two or more. In contrast, when examining the entire roster of confirmed planets in

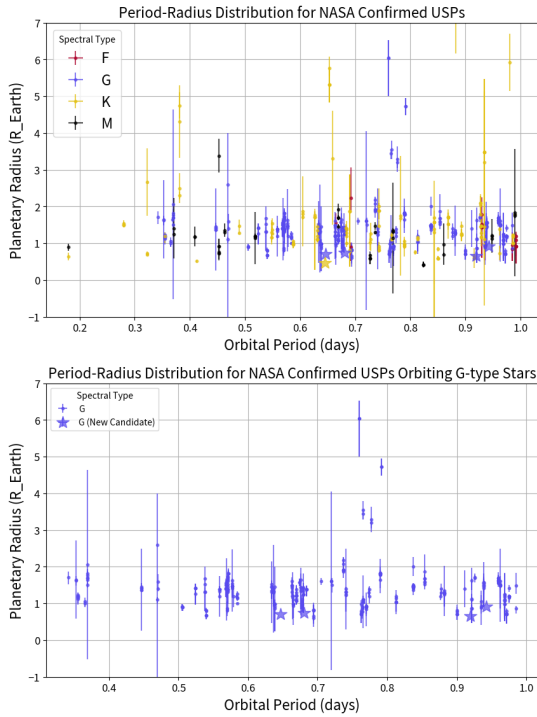


**Figure 15.** Period-Radius distribution of confirmed USPs in the NASA Exoplanet Archive. This figure illustrates the Period-Radius distribution of confirmed USP planets from the NASA Exoplanet Archive. The USPs orbiting host stars of types F, G, K, and M are color-coded in red, green, yellow, and black, respectively. Existing known USPs are denoted with circles, while our five new candidates are highlighted with stars for clear differentiation. (a) K00446.c, with a planetary radius of  $0.461R_{\oplus}$ , stands as the second smallest USP across NASA confirmed exoplanets, encompassing all host star types. (b) The chart highlights K01821.b, K01522.c, and K03404.b as among the smallest USPs orbiting G-type stars. Moreover, K01821.b, with a radius of  $0.648R_{\oplus}$ , is also the second smallest USP orbiting G-type stars in the entirety of NASA’s confirmed USP catalog.

**Table 4.** Number of planet companions in multiplanet systems with an orbiting USP.

Companions	Kepler	NASA Confirmed Planets
0	86.2%	70.5%
>0	13.8%	29.5%
1	8.6%	18.0%
2+	5.2%	11.5%

the Kepler KOI catalog, the prevalence of multiplanet systems and systems with three planets drops to 13.8% and 5%, respectively. This disparity could suggest that the Kepler survey might underreport multiplanet systems. A detailed breakdown can be found in Table 4. Our recent discoveries contribute valuable data for subsequent studies on multiplanet systems and the planetary formation theories underpinning their existence.

Previous studies have frequently observed that USPs often coexist with longer-period planetary companions (Sanchis-Ojeda et al. 2014; Winn et al. 2018; Adams et al. 2020). As posited by (Sanchis-Ojeda et al. 2014), even USP systems devoid of known siblings likely house additional, non-transiting planets. Assuming multiplanet interactions—such as tidal migration or dynamical excitation—are crucial in positioning USPs onto their present orbits, the detection of

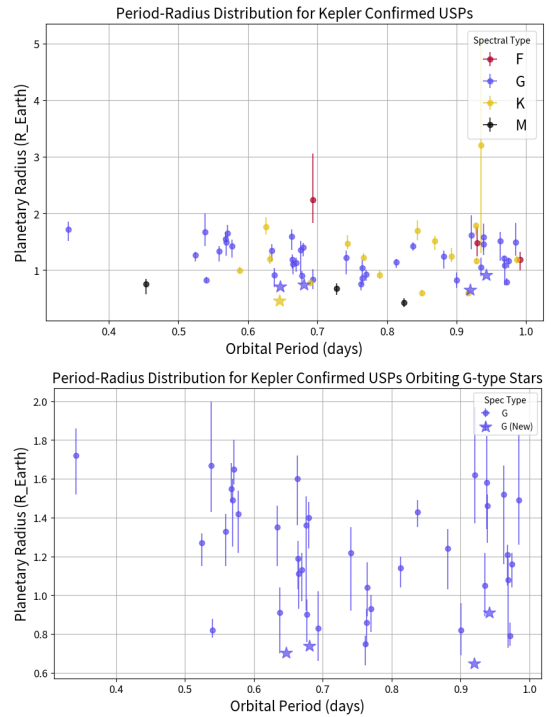


**Figure 16.** Period-Radius distribution of confirmed USPs in Kepler survey. This figure illustrates the Period-Radius distribution of confirmed USP planets from the NASA Exoplanet Archive. The USPs orbiting host stars of types F, G, K, and M are color-coded in red, green, yellow, and black, respectively. Existing known USPs are denoted with circles, while our five new candidates are highlighted with stars for clear differentiation. (a) K00446.c, with a planetary radius of  $0.461R_{\oplus}$ , stands as the second smallest USP across both Kepler and NASA confirmed exoplanets, encompassing all host star types. (b) The chart highlights K01821.b, K01522.c, and K03404.b as the three tiniest USPs orbiting G-type stars among all Kepler confirmed USPs. Moreover, K01821.b, with a radius of  $0.648R_{\oplus}$ , is also the second smallest USP orbiting G-type stars in the entirety of NASA’s confirmed USP catalog.

a USP would naturally suggest a comprehensive follow-up search for other, yet undetected, sibling planets in the same system. Furthermore, (Winn et al. 2018) emphasized that multiplanet systems encompassing a USP distinguish themselves from other Kepler multiplanet systems. While the typical Kepler multiplanet system without a USP exhibits period ratios ranging from 1.5 to 4 between adjacent planet pairs, systems with an inner USP characteristically maintain a larger period ratio, exceeding 3, between the USP and its adjacent outer companion. Our discoveries, as detailed in Table 5, resonate with these established observations.

## 6 CONCLUSION AND FUTURE WORK

In this study, we undertook a systematic search for ultra-short period transits within the Kepler dataset utilizing our innovative GPFC method. This approach fuses the power of GPU phase folding with the signal detection capability of a Convolutional Neural Network. One significant advantage of the GPFC method is its ability to process raw light curves from the Kepler survey independently of the TCE catalog. Credit to GPU parallelism and our meticulously calibrated CNN model, the GPFC system can analyze all confirmed planets in the KOI catalog within two days.

With the GPFC system we report the discovery of five sub-Earth-sized ultra-short-period exoplanets, namely K00446.c, K01821.b,

**Table 5.** Period and radius layout of the three-planetary systems with an orbiting USP. Currently known three-planetary systems in NASA Confirmed Exoplanets Archive are listed followed up our new three-planetary system candidates. The period and radius for each planet are shown to manifest the layout of the three-planetary systems.

NASA Confirmed Exoplanets		
Host Star	Stellar Type	Period (Radius) Ratio of Planets
Kepler-42	M	0.4530d (3.19 $R_{\oplus}$ ) : 1.214d (0.87 $R_{\oplus}$ ) : 1.865d (0.69 $R_{\oplus}$ )
YZ Cet	M	0.7520d (-) : 1.969d (-) : 4.658d (-)
TOI-431	K	0.4900d (1.28 $R_{\oplus}$ ) : 4.849d (-) : 12.46d (3.28 $R_{\oplus}$ )
K2-183	G	0.4690d (1.46 $R_{\oplus}$ ) : 10.793d (2.511 $R_{\oplus}$ ) : 22.63d (5.2 $R_{\oplus}$ )
CoRoT-7	G	0.8540d (1.58 $R_{\oplus}$ ) : 3.700d (-) : 8.966d (-)
EPIC-206024342	G	0.9116d (1.35 $R_{\oplus}$ ) : 4.508d (1.7 $R_{\oplus}$ ) : 14.641d (2.94 $R_{\oplus}$ )
New Candidates		
Host Star	Stellar Type	Period (Radius) Ratio of Planets
Kepler-158 (KIC4633570)	K	0.645091d (0.461 $R_{\oplus}$ ) : 16.709206d (2.27 $R_{\oplus}$ ) : 28.551582d (1.97 $R_{\oplus}$ )
Kepler-879 (KIC12266636)	G	0.646720d (0.704 $R_{\oplus}$ ) : 12.654896d (1.02 $R_{\oplus}$ ) : 33.385618d (2.48 $R_{\oplus}$ )

K01522.c, K03404.b, and K04978.b. Notably, K00446.c, with a radius of 0.461  $R_{\oplus}$ , ranks as the second smallest USP identified to date. K01821.b is a unique USP orbiting a G dwarf which stands out as the second smallest of its category. In addition, three of our identified candidates, K01821.b, K01522.c and K03404.b, are smaller than any known confirmed USPs orbiting G dwarfs in the Kepler record.

All five candidates coexist in their respective host systems with other known planets. Additionally, both K00446.c and K01522.c are part of 3-planet multiplanetary systems. These discoveries resonate with USP formation theories, suggesting that outer planets within the host system may play an important role in positioning the innermost USP planet in a close orbit to the host.

The discovery of these sub-Earth-sized planets demonstrates the effectiveness of the GPFC method for detecting small exoplanets. The GPFC method is generic and can be applied to longer period ranges and many other transit surveys. We see great potential in its broader applications and we aim to explore these in future studies.

## ACKNOWLEDGEMENTS

This research has made use of NASA's Astrophysics Data System and the NASA Exoplanet Archive, which is operated by the California Institute of Technology under contract with NASA's Exoplanet Exploration Program. The data presented in this paper includes information collected by the *Kepler* mission. The funding for the *Kepler* mission is provided by NASA's Science Mission Directorate.

## DATA AVAILABILITY

The Kepler light curves used in this study are available at the following link: <https://exoplanetarchive.ipac.caltech.edu/cgi-bin/TblView/nph-tblView?app=ExoTbls&config=cumulative>. Additionally, a table listing all confirmed physically periodic sources will be made available online.

## REFERENCES

Adams E. R., et al., 2020, Ultra Short Period Planets in K2 III: Neighbors are Common with 13 New Multi-Planet Systems and 10 Newly Vali-

- dated Planets in Campaigns 0-8, 10, [doi:10.48550/ARXIV.2011.11698](https://arxiv.org/abs/2011.11698), <https://arxiv.org/abs/2011.11698>
- Adams E. R., et al., 2021, *The Planetary Science Journal*, 2, 152
- Boss A. P., 1998, *The Astrophysical Journal*, 503, 923
- Claret, A. Bloemen, S. 2011, *A&A*, 529, A75
- Coughlin J. L., et al., 2016, *The Astrophysical Journal Supplement Series*, 224, 12
- D'Antona F., Mazzitelli I., 1994, *Astrophysical Journal Supplement Series*, 90, 467
- Dawson R. I., Johnson J. A., 2018, *Annual Review of Astronomy and Astrophysics*, 56, 175
- Gaia Collaboration et al., 2021, *A&A*, 649, A1
- Goodman J. R., Weare J., 2010, *Communications in Applied Mathematics and Computational Science*, 5, 65
- Hipke M., Heller R., 2019, TLS: Transit Least Squares, Astrophysics Source Code Library, record ascl:1910.007 (ascl:1910.007)
- Jenkins J. M., et al., 2010, *The Astrophysical Journal*, 713, L87
- Jia S., Spruit H. C., 2016, *Monthly Notices of the Royal Astronomical Society*, 465, 149
- Kingma D. P., Ba J., 2014, Adam: A Method for Stochastic Optimization, [doi:10.48550/ARXIV.1412.6980](https://arxiv.org/abs/1412.6980), <https://arxiv.org/abs/1412.6980>
- Kipping D. M., 2013, *Monthly Notices of the Royal Astronomical Society*, 435, 2152
- Mandel K., Agol E., 2002, *The Astrophysical Journal*, 580, L171
- Owen J. E., Kollmeier J. A., 2019, *Monthly Notices of the Royal Astronomical Society*, 487, 3702
- Palla F., Stahl S., 1991, *Astrophysical Journal*, 375, 288
- Rappaport S., Sanchis-Ojeda R., Rogers L. A., Levine A., Winn J. N., 2013, *The Astrophysical Journal*, 773, L15
- Sanchis-Ojeda R., Rappaport S., Winn J. N., Kotson M. C., Levine A., Mellah I. E., 2014, *The Astrophysical Journal*, 787, 47
- Shahaf S., Zackay B., Mazeh T., Faigler S., Ivashenko O., 2022, *MNRAS*, 513, 2732
- Shallue C. J., Vanderburg A., 2018, *The Astronomical Journal*, 155, 94
- Smith A. M. S., et al., 2017, *Monthly Notices of the Royal Astronomical Society*, 474, 5523
- Vanderburg A., Johnson J. A., 2014, *Publications of the Astronomical Society of the Pacific*, 126, 948
- Wang K., Wang K., Ge J., Zhao Y., Willis K., 2023, The GPU Phase Folding and Deep Learning Method for Detecting Exoplanet Transits ([arXiv:2312.02063](https://arxiv.org/abs/2312.02063))
- Winn J. N., Sanchis-Ojeda R., Rappaport S., 2018, *New Astronomy Reviews*, 83, 37

**APPENDIX A: ADDITIONAL FIGURES**

This paper has been typeset from a  $\text{\TeX/L\AA\TeX}$  file prepared by the author.



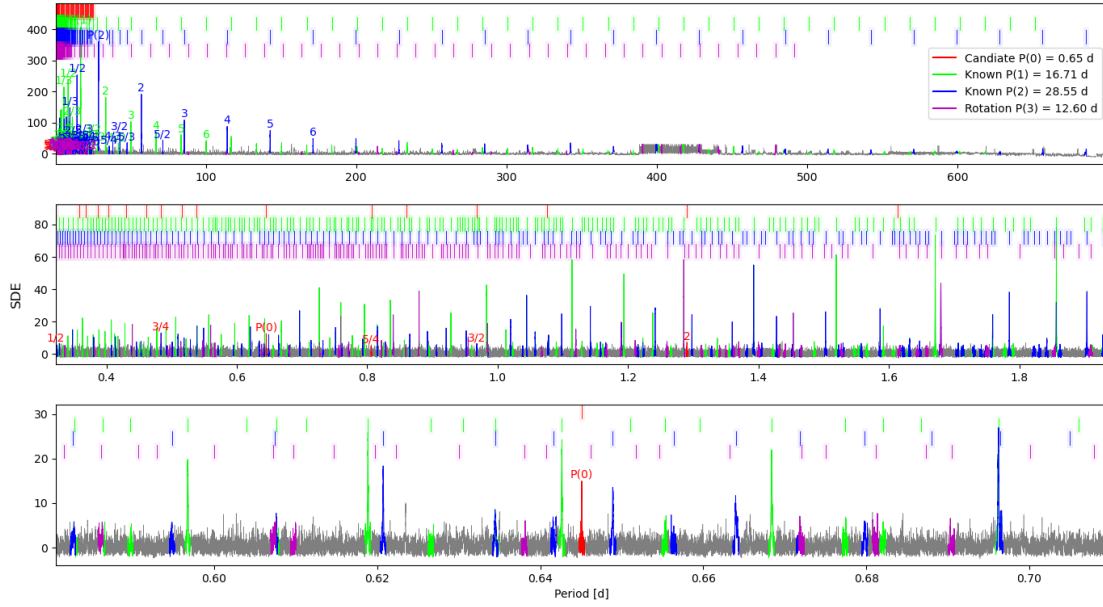


**Figure A1.** BLS Peaks check and Known Sibling Transit Harmonics Check for candidate K00446.c. Harmonics of the orbital period for the host star’s known orbiting planets are color-coded in green and blue. Harmonics associated with the rotational period of the variable star are indicated in purple. Meanwhile, the harmonics of the orbital period of the new candidate are marked in red. This visualization confirms that the orbital period of the new candidate does not coincide with the periods of the already known planets or the rotational period of the star.

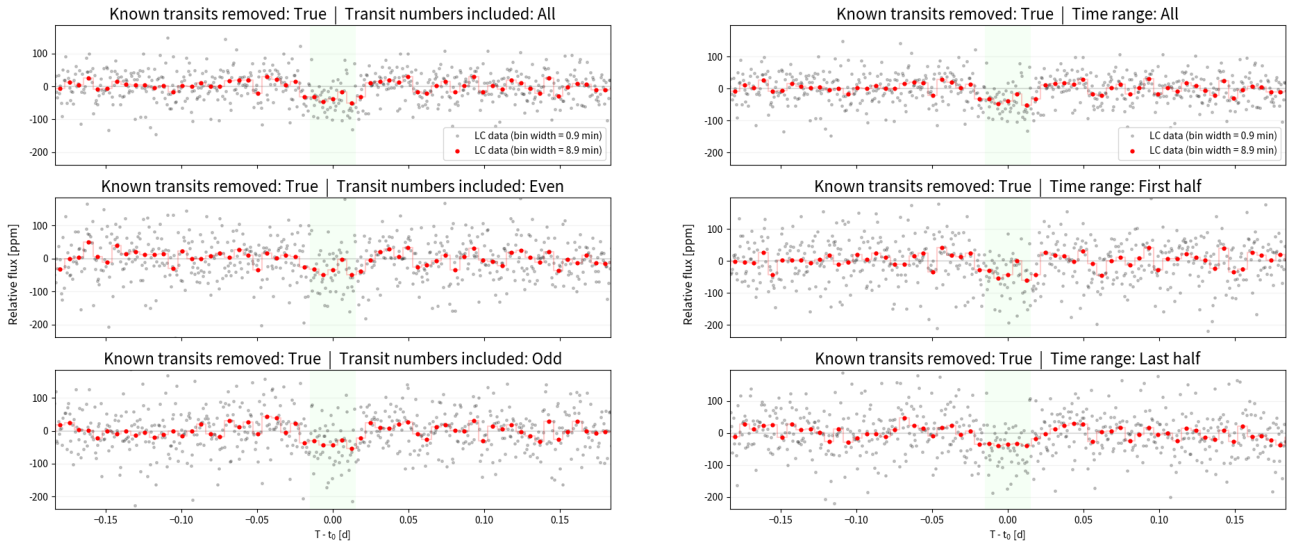


**Figure A2.** Even-odd and left-right-half transit check for candidate K00446.c. This test verifies that the transit signals of the new candidates remain consistent across both subsets of the light curve time sequence.

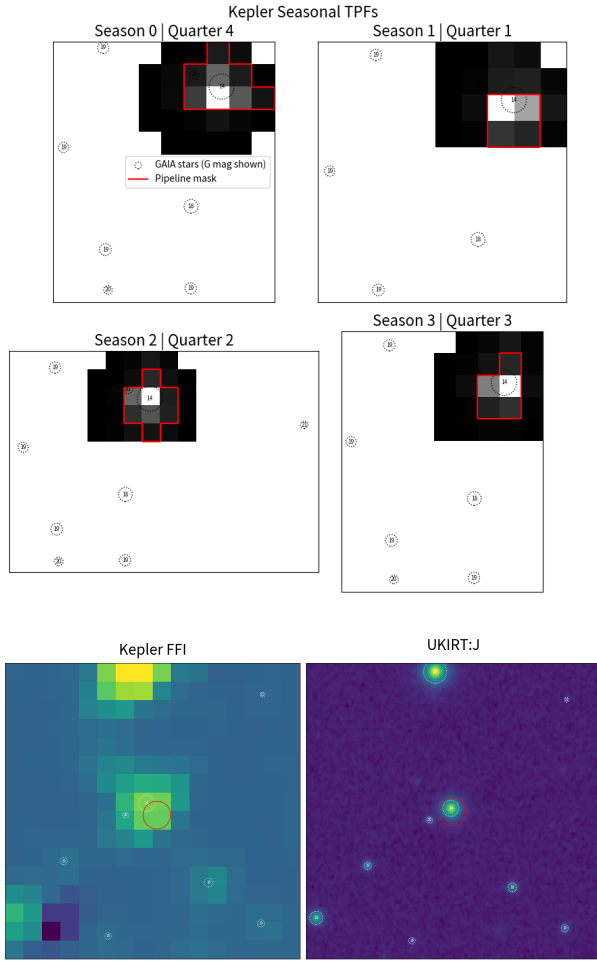


**Figure A3.** The seasonal TPFs, FFI, and UKIRT-J plots for candidate K00446.c. The upper four seasonal TPFs show the position and apparent magnitude of the neighboring stars. Stars located within the highlighted red aperture exhibit significantly higher magnitudes, indicating lower brightness. This ensures that they do not contribute to any interference with the detected transit signal. The FFI and UKIRT-J images below allow a visual inspection of the broader view of the field with no contamination exhibited.

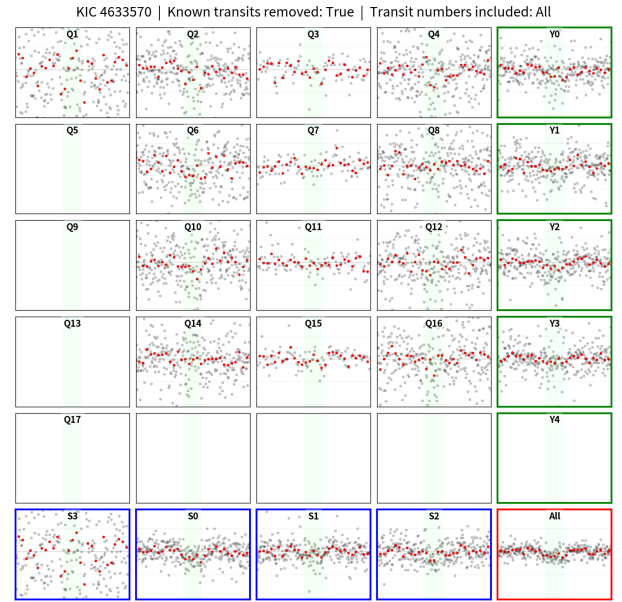


**Figure A4.** Quarterly Rotation Check for candidate K00446.c. This test confirms the consistency of the transit signals across different quarters.

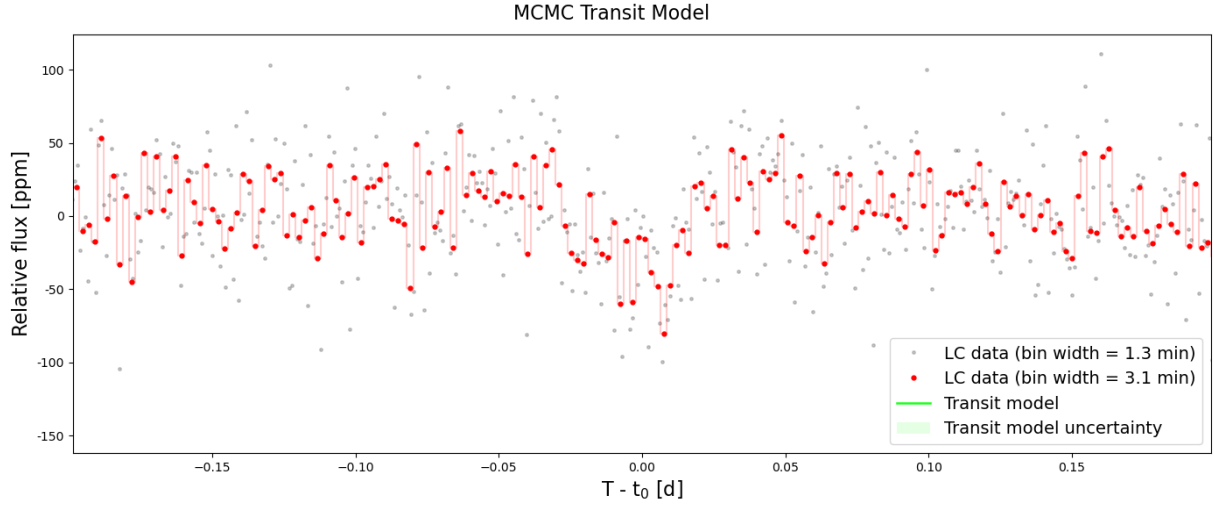


**Figure A5.** The MCMC best-fitting plot for candidate K00446.c. The MCMC best-fitting plot: The flux data are folded with the transit period and subsequently binned into 1.3-minute bins (represented by grey dots) and 3.1-minute bins (represented by red lines). The green curve represents the optimal transit model, with the shaded green area within the transit window illustrating the uncertainty of the model.

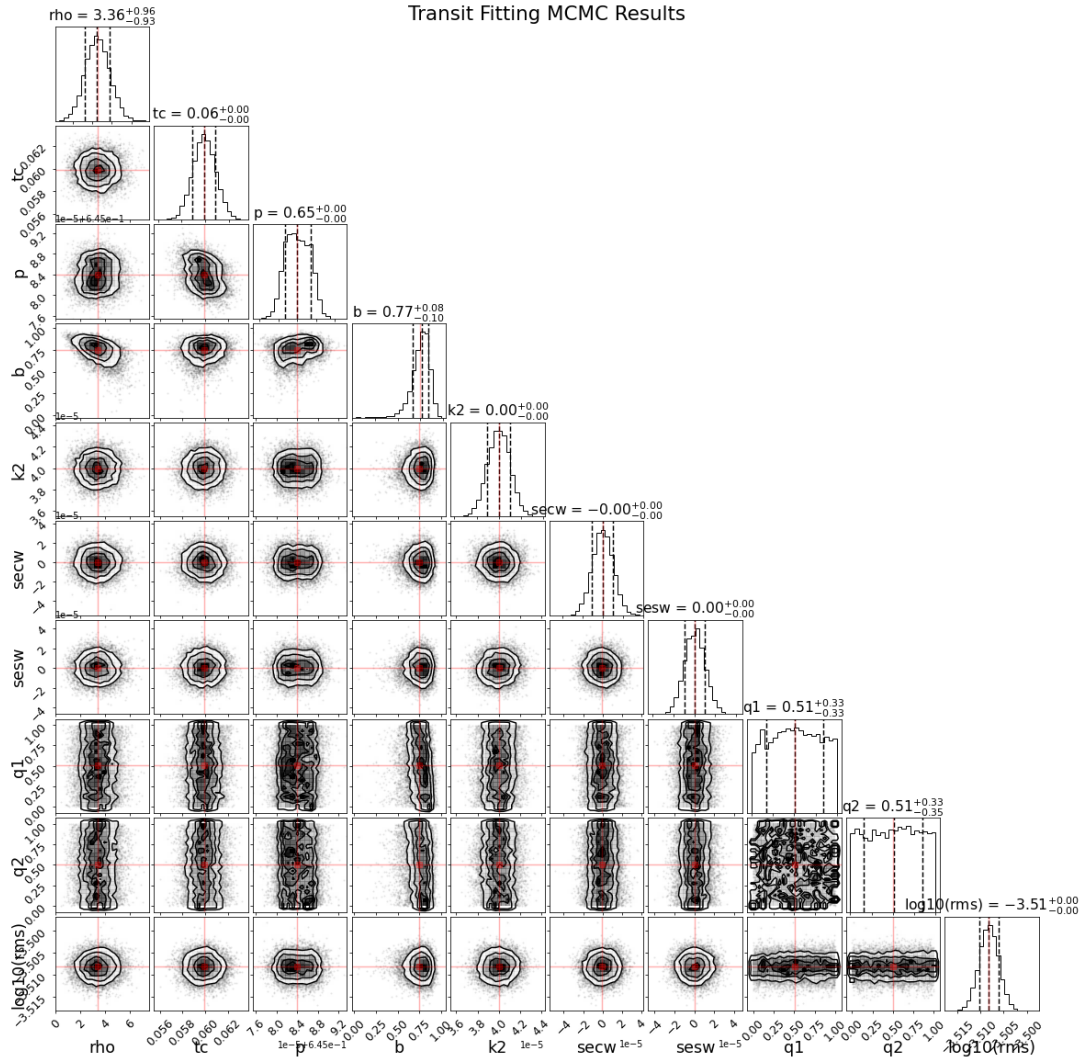


**Figure A6.** The corner plot for candidate K00446.c. Indicated are the stellar density ( $\rho$ ), time of central transit ( $t_c$ ), orbital period ( $p$ ), impact parameter ( $b$ ), square of the radius ratio ( $k_2$ ), orbit periastron and eccentricity params ( $secw$  and  $sesw$ ), limb-darkening coefficients ( $q_1$  and  $q_2$ ), as well as the logarithm base 10 of the white noise level in the data ( $\log_{10}(rms)$ ). The red lines represent the most likely values, while the dashed lines reflect the one sigma limits.

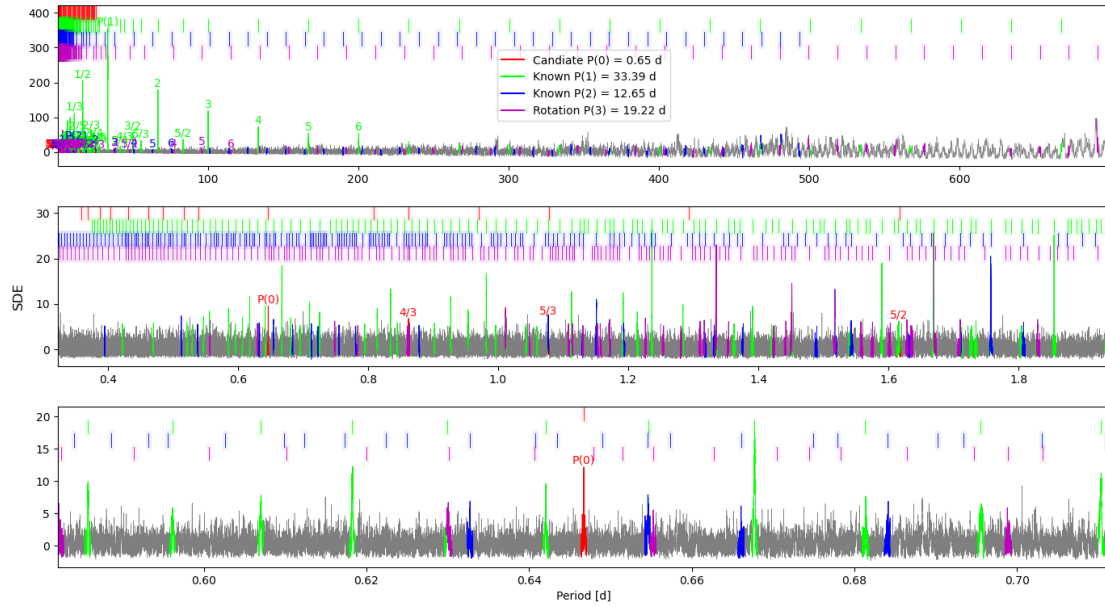


**Figure A7.** BLS Peaks check and Known Sibling Transit Harmonics Check for candidate K01522.c. Harmonics of the orbital period for the host star’s known orbiting planets are color-coded in green and blue. Harmonics associated with the rotational period of the variable star are indicated in purple. Meanwhile, the harmonics of the orbital period of the new candidate are marked in red. This visualization confirms that the orbital period of the new candidate does not coincide with the periods of the already known planets or the rotational period of the star.

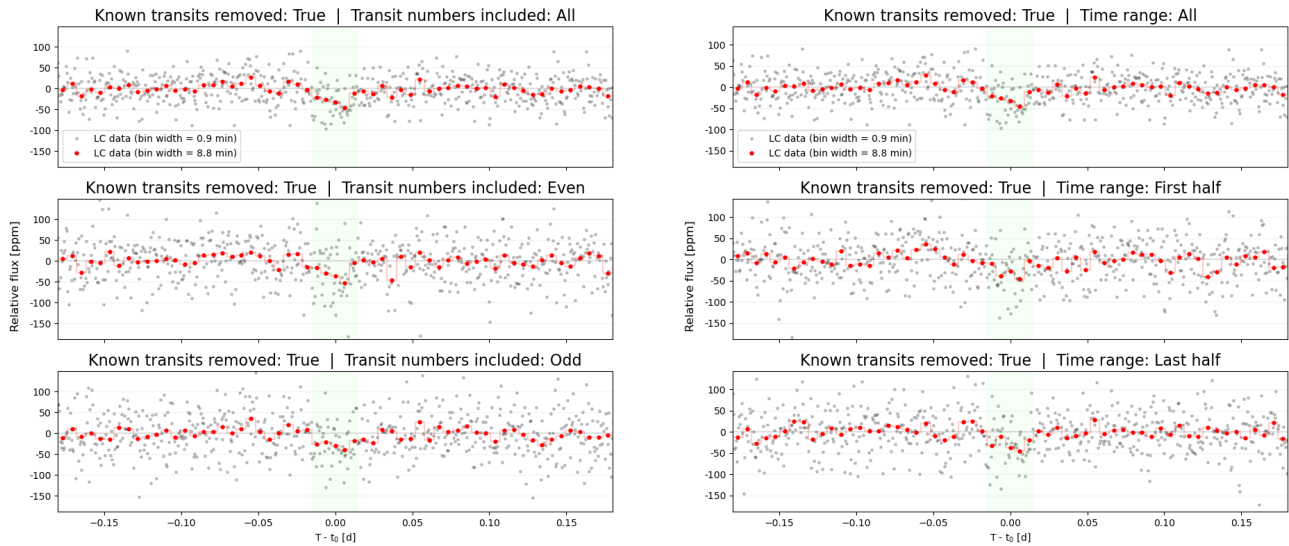


**Figure A8.** Even-odd and left-right-half transit check for candidate K01522.c. This test verifies that the transit signals of the new candidates remain consistent across both subsets of the light curve time sequence.



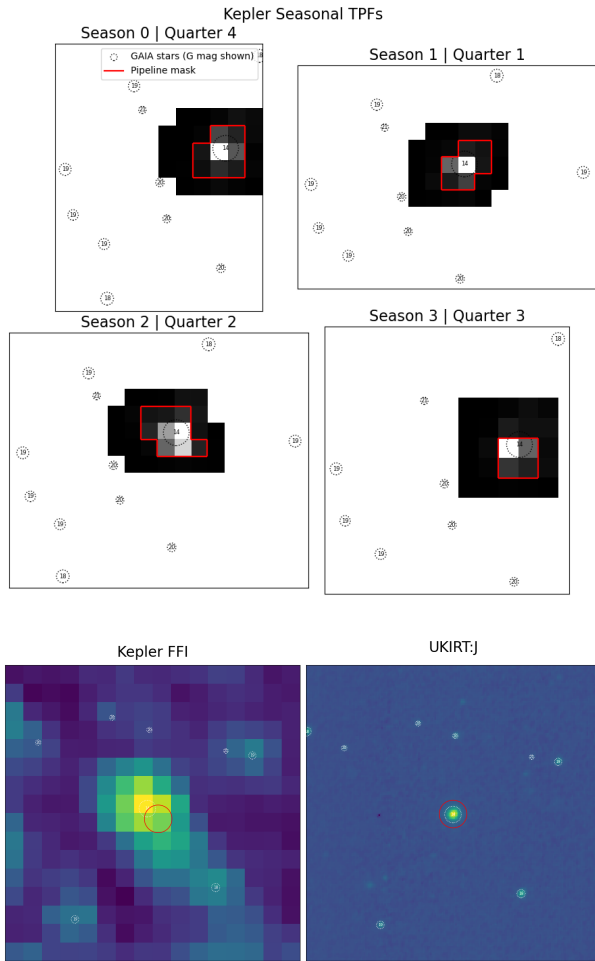


**Figure A9.** The seasonal TPFs, FFI, and UKIRT-J plots for candidate K01522.c. The upper four seasonal TPFs show the position and apparent magnitude of the neighboring stars. Stars located within the highlighted red aperture exhibit significantly higher magnitudes, indicating lower brightness. This ensures that they do not contribute to any interference with the detected transit signal. The FFI and UKIRT-J images below allow a visual inspection of the broader view of the field with no contamination exhibited.

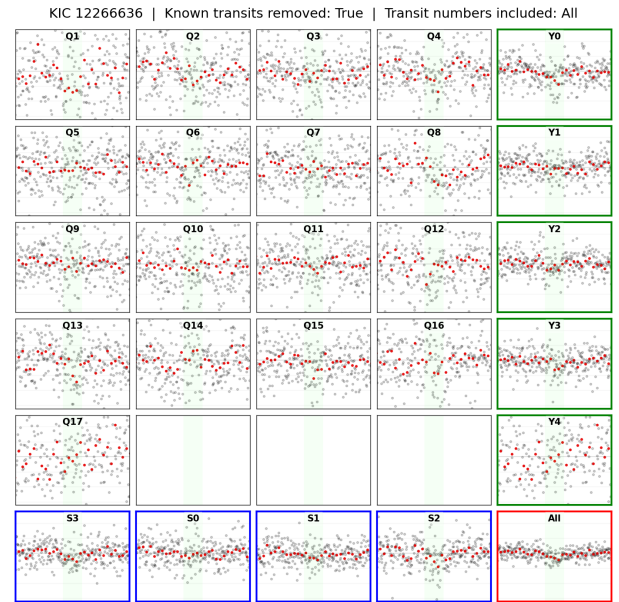


**Figure A10.** Quarterly Rotation Check for candidate K01522.c. This test confirms the consistency of the transit signals across different quarters.

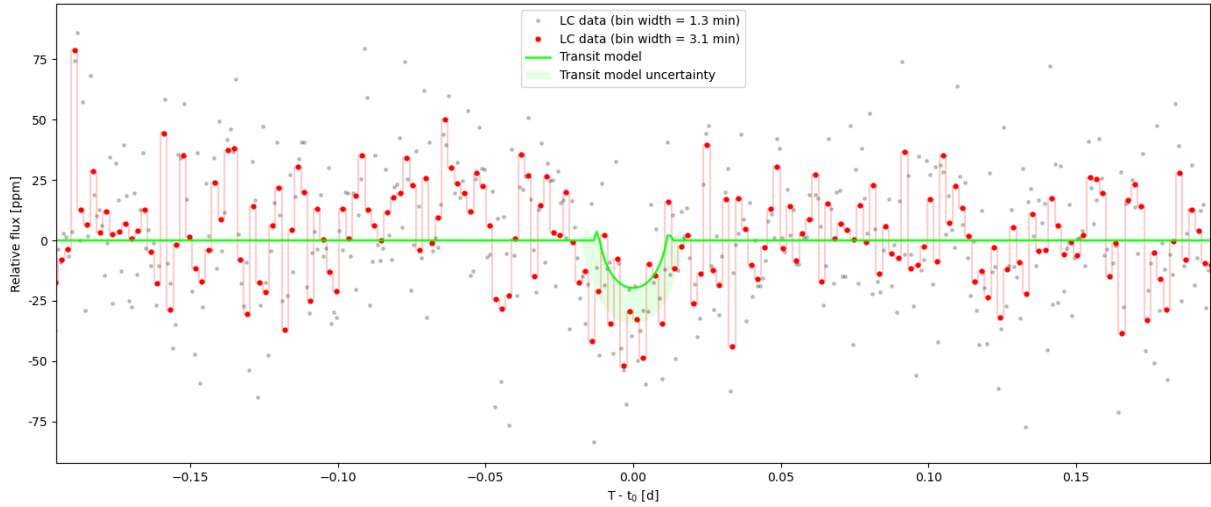


**Figure A11.** The MCMC best-fitting plot for candidate K01522.c. The MCMC best-fitting plot: The flux data are folded with the transit period and subsequently binned into 1.3-minute bins (represented by grey dots) and 3.1-minute bins (represented by red lines). The green curve represents the optimal transit model, with the shaded green area within the transit window illustrating the uncertainty of the model.

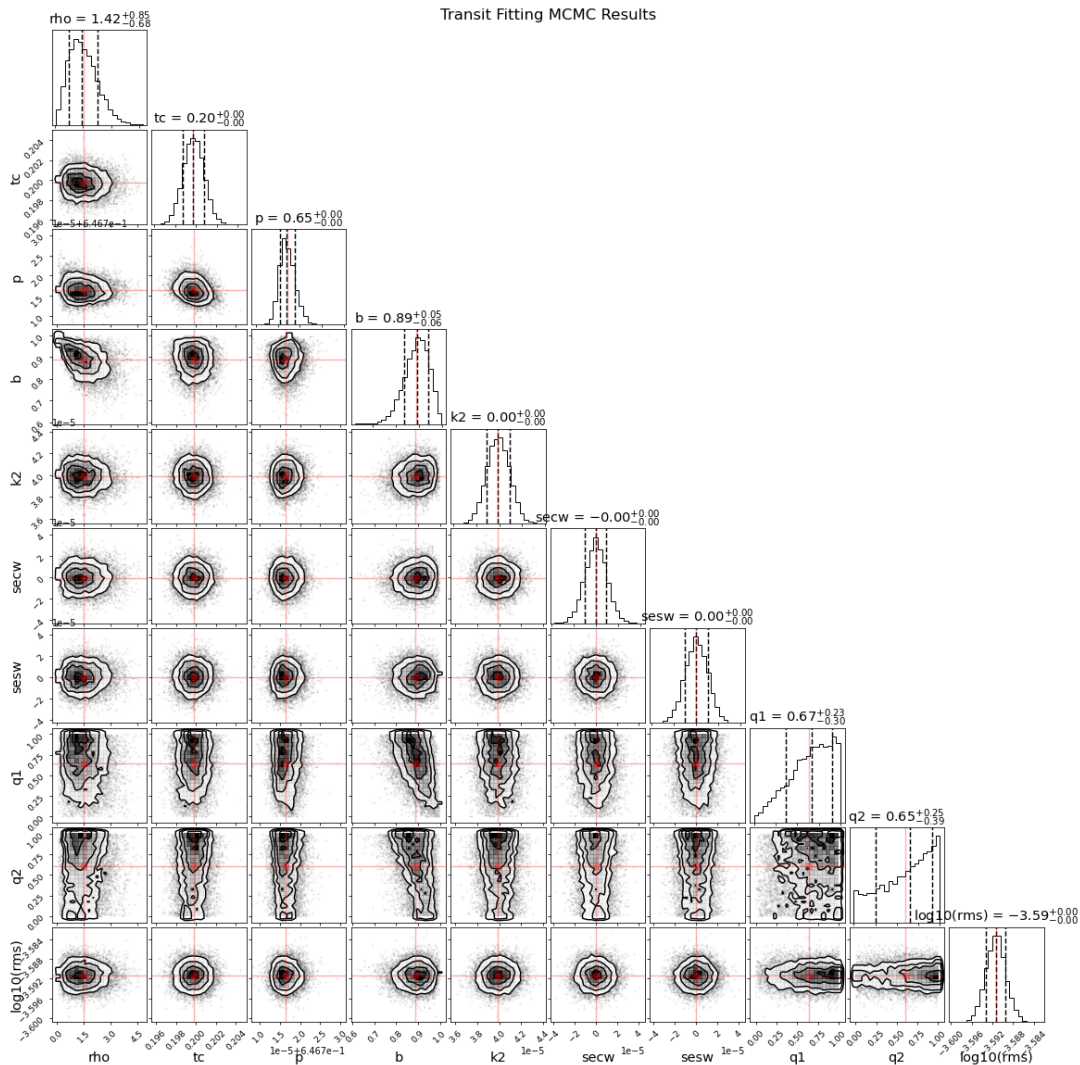


**Figure A12.** The corner plot for candidate K01522.c. Indicated are the stellar density ( $\rho$ ), time of central transit ( $t_c$ ), orbital period ( $p$ ), impact parameter ( $b$ ), square of the radius ratio ( $k_2$ ), orbit periastron and eccentricity params ( $secw$  and  $sesw$ ), limb-darkening coefficients ( $q_1$  and  $q_2$ ), as well as the logarithm base 10 of the white noise level in the data ( $\log_{10}(rms)$ ). The red lines represent the most likely values, while the dashed lines reflect the one sigma limits.

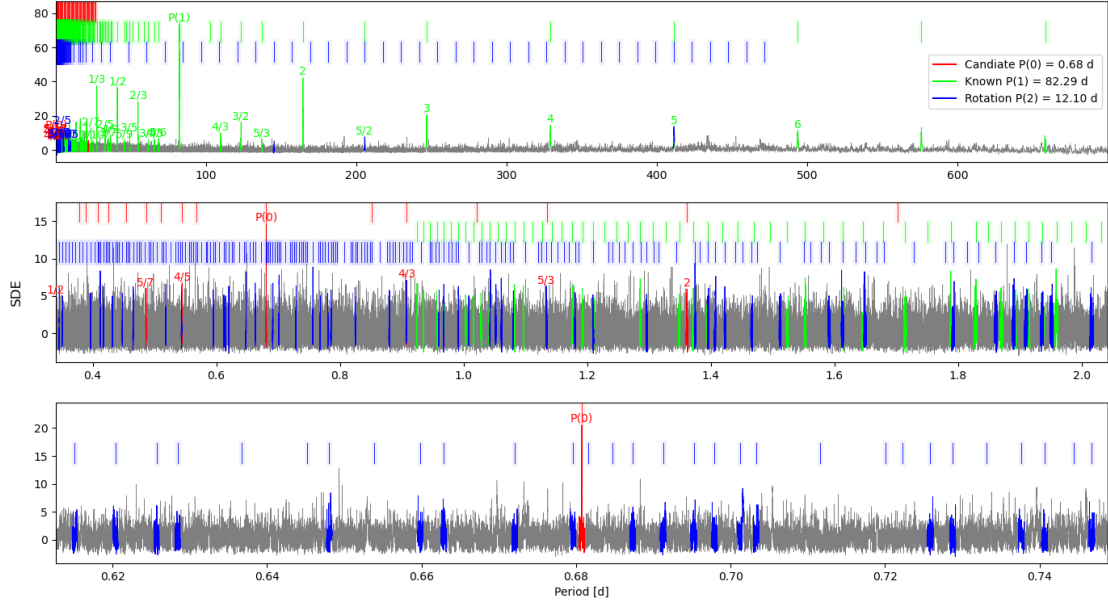


**Figure A13.** BLS Peaks check and Known Sibling Transit Harmonics Check for candidate K03404.b. Harmonics of the orbital period for the host star’s known orbiting planet are color-coded in green. Harmonics associated with the rotational period of the variable star are indicated in blue. Meanwhile, the harmonics of the orbital period of the new candidate are marked in red. This visualization confirms that the orbital period of the new candidate does not coincide with the periods of the already known planet or the rotational period of the star.

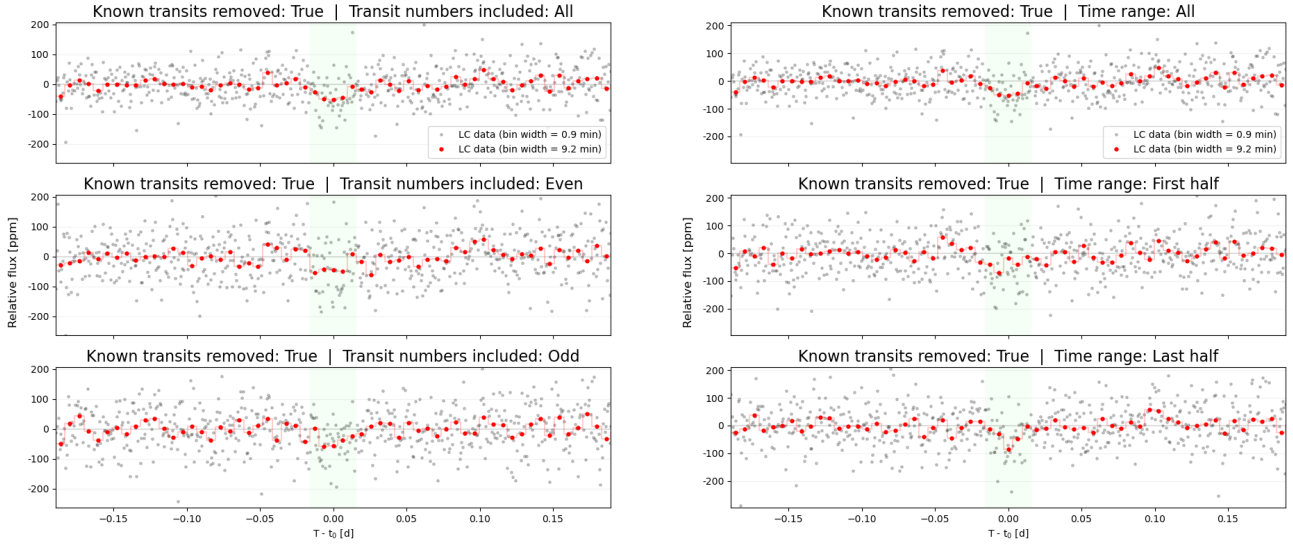


**Figure A14.** Even-odd and left-right-half transit check for candidate K03404.b. This test verifies that the transit signals of the new candidates remain consistent across both subsets of the light curve time sequence.

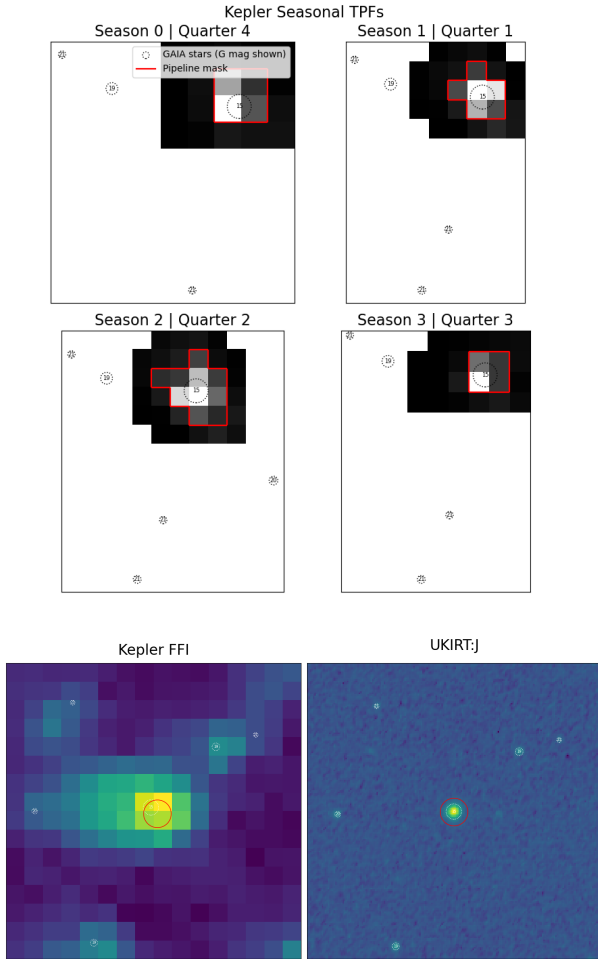


**Figure A15.** The seasonal TPFs, FFI, and UKIRT-J plots for candidate K03404.b. The upper four seasonal TPFs show the position and apparent magnitude of the neighboring stars. Stars located within the highlighted red aperture exhibit significantly higher magnitudes, indicating lower brightness. This ensures that they do not contribute to any interference with the detected transit signal. The FFI and UKIRT-J images below allow a visual inspection of the broader view of the field with no contamination exhibited.

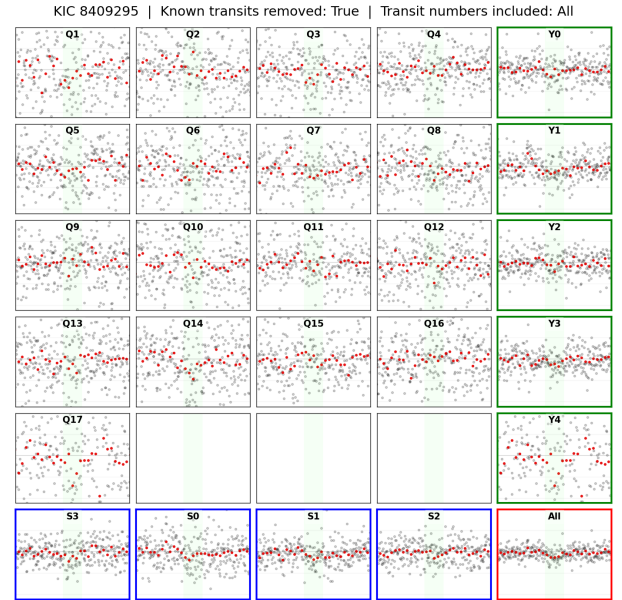


**Figure A16.** Quarterly Rotation Check for candidate K03404.b. This test confirms the consistency of the transit signals across different quarters.



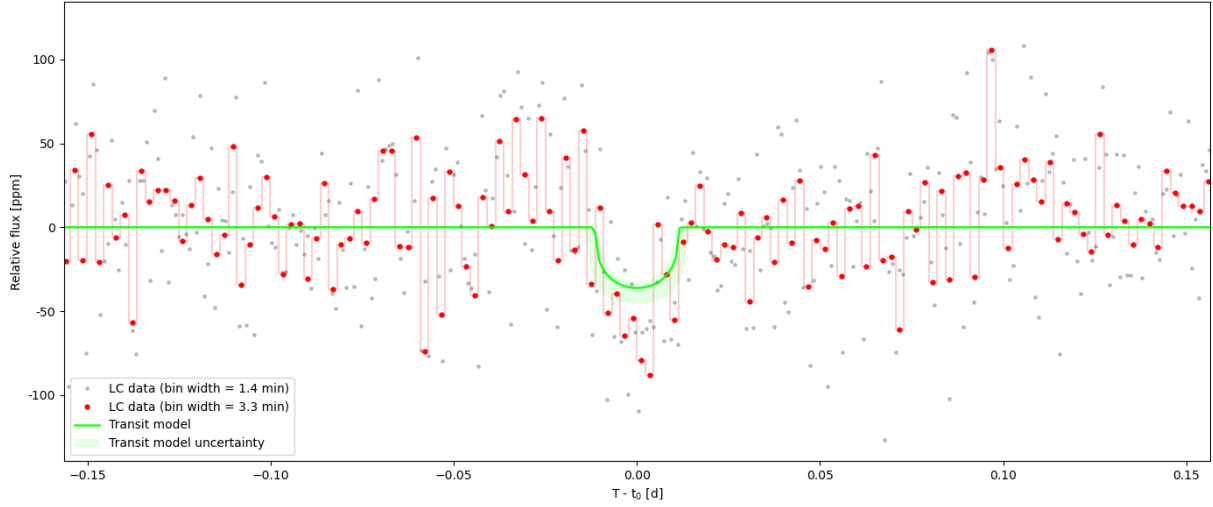


**Figure A17.** The MCMC best-fitting plot for candidate K03404.b. The MCMC best-fitting plot: The flux data are folded with the transit period and subsequently binned into 1.4-minute bins (represented by grey dots) and 3.3-minute bins (represented by red lines). The green curve represents the optimal transit model, with the shaded green area within the transit window illustrating the uncertainty of the model.

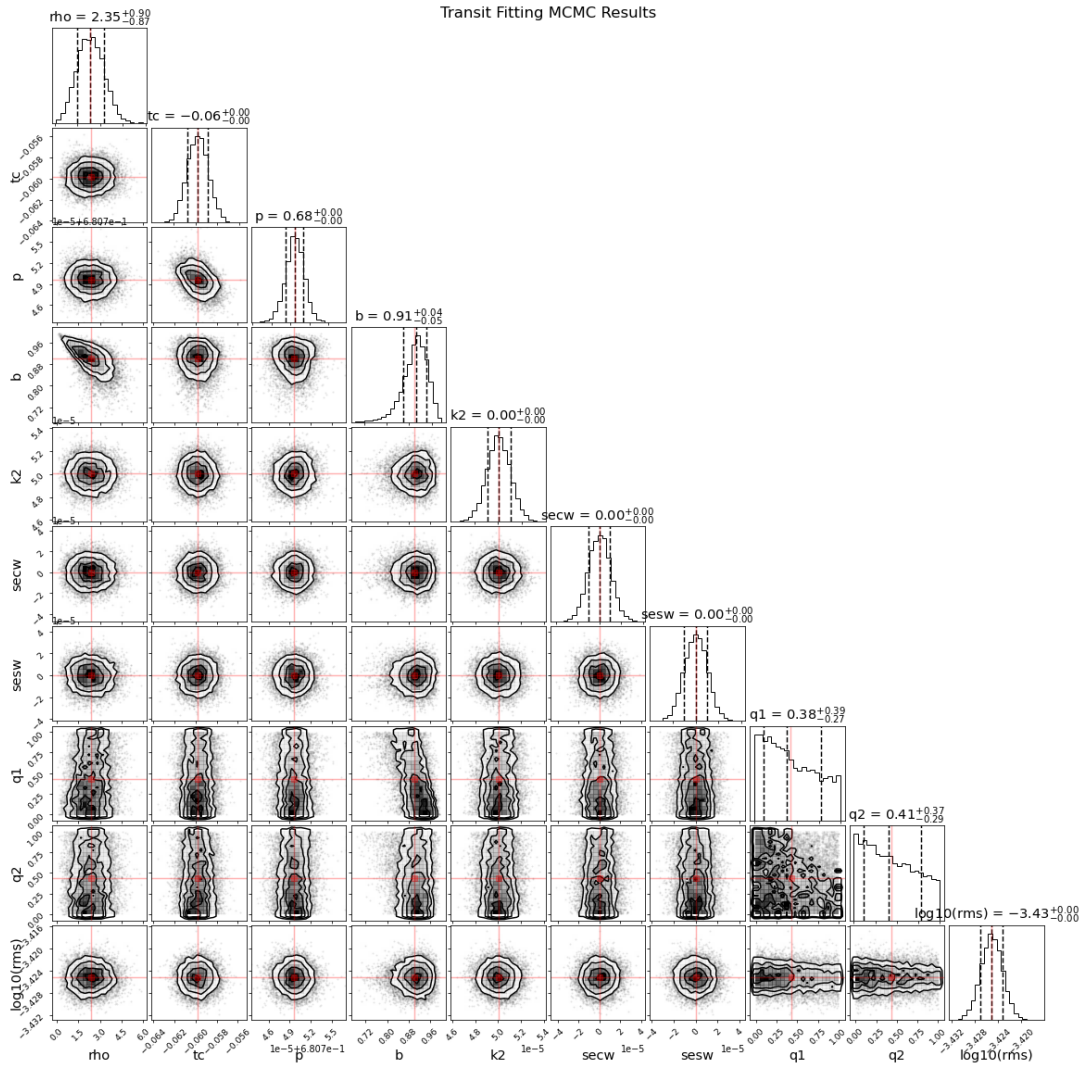


**Figure A18.** The corner plot for candidate K03404.b. Indicated are the stellar density ( $\rho$ ), time of central transit ( $t_c$ ), orbital period ( $p$ ), impact parameter ( $b$ ), square of the radius ratio ( $k_2$ ), orbit periastron and eccentricity params ( $secw$  and  $sesw$ ), limb-darkening coefficients ( $q_1$  and  $q_2$ ), as well as the logarithm base 10 of the white noise level in the data ( $\log_{10}(rms)$ ). The red lines represent the most likely values, while the dashed lines reflect the one sigma limits.



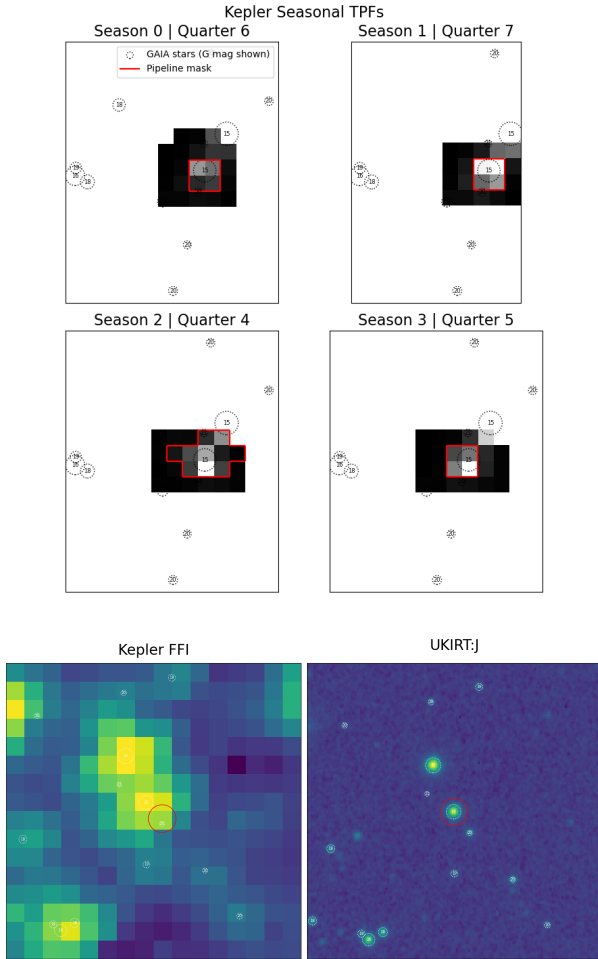


**Figure A21.** The seasonal TPFs, FFI, and UKIRT-J plots for candidate K04978.b. The upper four seasonal TPFs show the position and apparent magnitude of the neighboring stars. Stars located within the highlighted red aperture exhibit significantly higher magnitudes, indicating lower brightness. This ensures that they do not contribute to any interference with the detected transit signal. The FFI and UKIRT-J images below allow a visual inspection of the broader view of the field with no contamination exhibited.

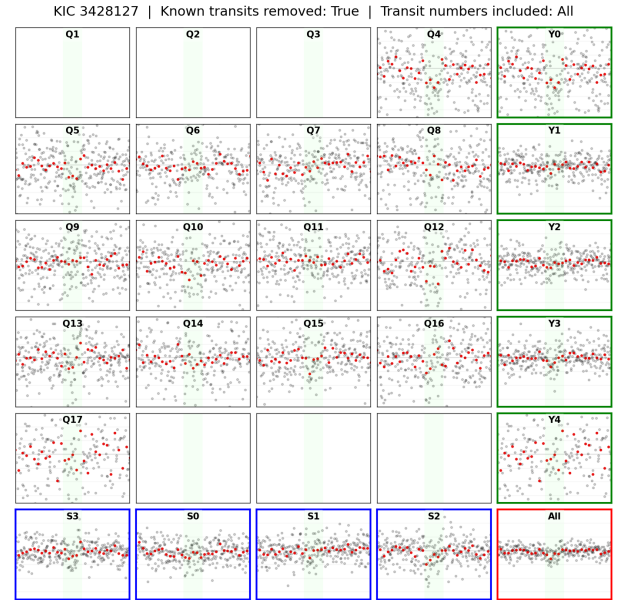


**Figure A22.** Quarterly Rotation Check for candidate K04978.b. This test confirms the consistency of the transit signals across different quarters.

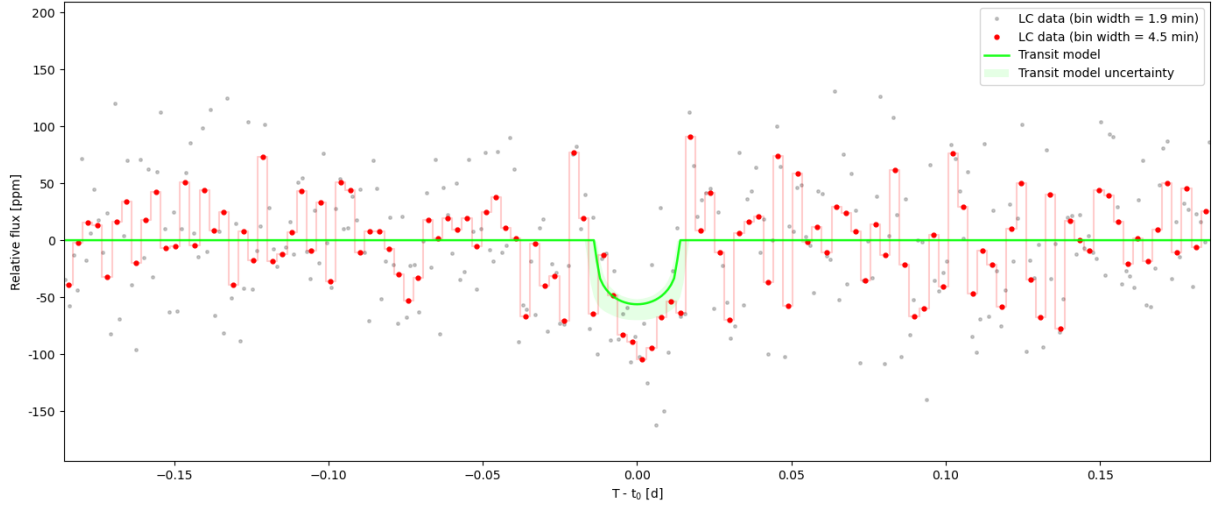


**Figure A23.** The MCMC best-fitting for candidate K04978.b. The flux data are folded with the transit period and subsequently binned into 1.9-minute bins (represented by grey dots) and 4.5-minute bins (represented by red lines). The green curve represents the optimal transit model, with the shaded green area within the transit window illustrating the uncertainty of the model.

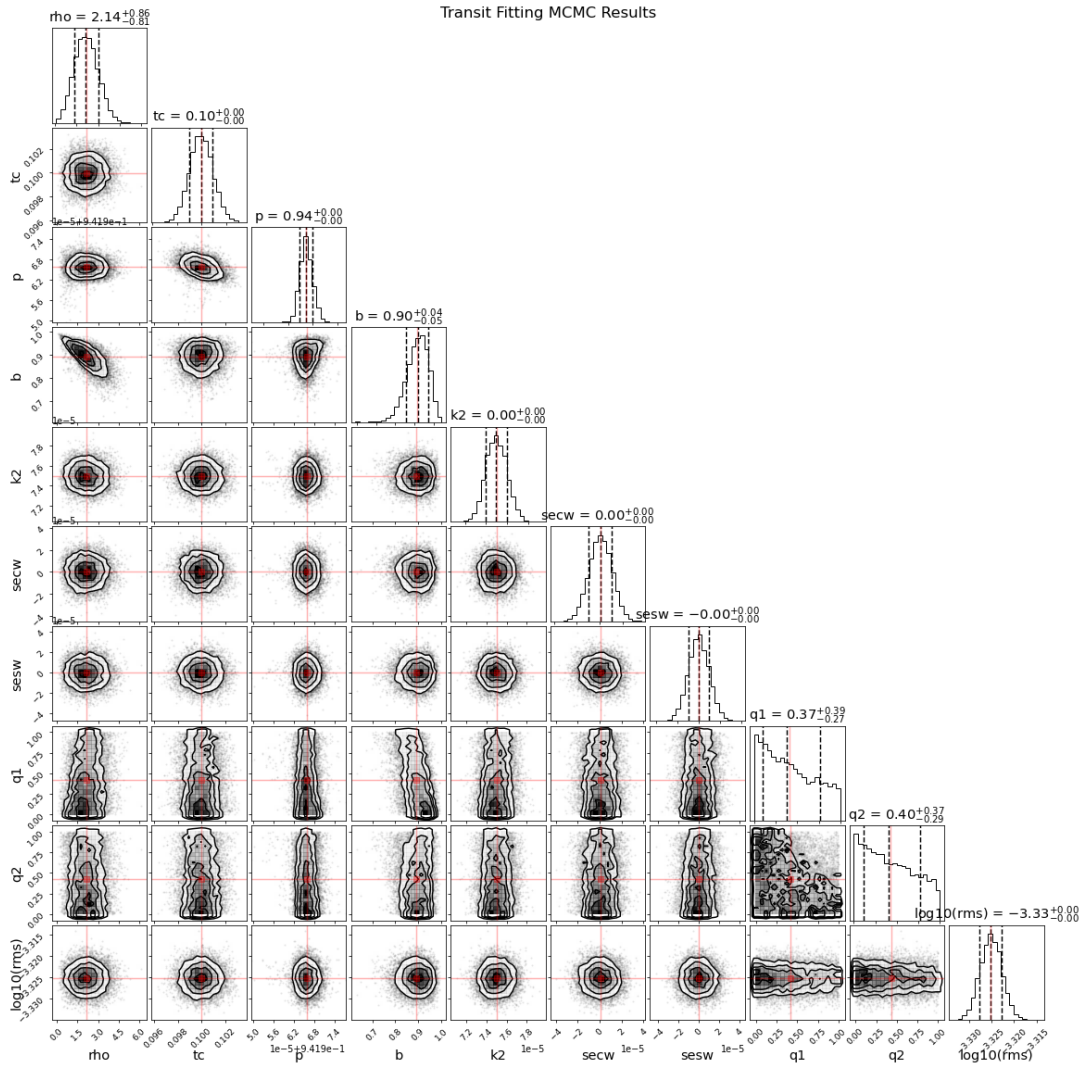


**Figure A24.** The corner plot for candidate K04978.b. Indicated are the stellar density ( $\rho$ ), time of central transit ( $t_c$ ), orbital period ( $p$ ), impact parameter ( $b$ ), square of the radius ratio ( $k_2$ ), orbit periastron and eccentricity params ( $secw$  and  $sesw$ ), limb-darkening coefficients ( $q_1$  and  $q_2$ ), as well as the logarithm base 10 of the white noise level in the data ( $\log_{10}(rms)$ ). The red lines represent the most likely values, while the dashed lines reflect the one sigma limits.